Earthquake Recurrence Model for the Colombia–Ecuador Subduction Zone Constrained from Seismic and Geodetic Data, Implication for PSHA

Judith Mariniere*[1], Céline Beauval[1], Jean-Mathieu Nocquet[2,3], Mohamed Chlieh[1], and Hugo Yepes[4]

ABSTRACT

Probabilistic seismic hazard assessment relies on long-term earthquake forecasts and ground-motion models. Our aim is to improve earthquake forecasts by including information derived from geodetic measurements, with an application to the Colombia–Ecuador megathrust. The annual rate of moment deficit accumulation at the interface is quantified from geodetically based interseismic coupling models. We look for Gutenberg–Richter recurrence models that match both past seismicity rates and the geodetic moment deficit rate, by adjusting the maximum magnitude. We explore the uncertainties on the seismic rates (*a*- and *b*-values, shape close to M_{max}) and on the geodetic moment deficit rate to be released seismically. A distribution for the maximum magnitude M_{max} bounding a series of earthquake recurrence models is obtained for the Colombia–Ecuador megathrust. Models associated with M_{max} values compatible with the extension of the interface segment are selected. We show that the uncertainties mostly influencing the moment-balanced recurrence model are the fraction of geodetic moment released through aseismic processes and the form of the Gutenberg–Richter model close to M_{max}. We combine the computed moment-balanced recurrence models with a ground-motion model, to obtain a series of uniform hazard spectra representative of uncertainties at one site on the coast. Considering the recent availability of a massive quantity of geodetic data, our approach could be used in other well-instrumented regions of the world.

KEY POINTS

- Our aim is to improve earthquake recurrence models for probabilistic seismic-hazard assessment, by including information derived from geodesy.
- The estimation of aseismic transient slip and the form of recurrence models close to M_{max} play a major role.
- Moment-balanced earthquake recurrence models lead to more realistic seismic hazard levels.

INTRODUCTION

The Nazca–South American subduction zone is among the most seismically active convergent margins in the world. Between latitudes −3° and 2° (Fig. 1), the oceanic Nazca plate subducts at a rate of ∼47 mm/yr below the North Andean Sliver (NAS), a continental domain moving independently from South America (Pennington, 1981; Nocquet *et al.*, 2014; Alvarado *et al.*, 2016). This subduction segment has experienced six large megathrust earthquakes, since the beginning of the twentieth century: in 1906 (M_s ∼ 8.6, Ye *et al.*, 2016), 1942 ($M_{w(ISC-GEM)}$ 7.8, magnitude from International Seismological Centre–Global Earthquake Model), 1958 ($M_{w(ISC–GEM)}$ 7.6), 1979 ($M_{w(GlobalCMT)}$ 8.1, magnitude from the Global Centroid Moment Tensor), 1998 ($M_{w(GlobalCMT)}$ 7.1), and 2016 ($M_{w(GlobalCMT)}$ 7.8) (Fig. 1). In this area, the coast lies ∼15 to ∼40 km directly above the rupture area of megathrust earthquakes and is, particularly, exposed to strong shaking during large events. For instance, horizontal peak ground accelerations (PGAs) recorded at stations above the 2016 M_w 7.8 Pedernales rupture plane exceeded 1.0*g* (Beauval *et al.*, 2017), along with significant damages to buildings and more than 670 deaths (Secretaria de Gestion de Riesgos [SGR], 2016).

1. ISTerre, IRD, Université Grenoble Alpes, Université Savoie Mont Blanc, CNRS, Université Gustave Eiffel, Grenoble, France, https://orcid.org/0000-0003-3706-6196 (JM); https://orcid.org/0000-0002-2614-7268 (CB); https://orcid.org/0000-0003-2252-2187 (MC); 2. Université Côte d'Azur, IRD, CNRS, Observatoire de la Côte d'Azur, Géoazur, Valbonne, France, https://orcid.org/0000-0002-3436-9354 (JMN); 3. Université de Paris, Institut de Physique du Globe de Paris, CNRS, Paris, France; 4. Escuela Politécnica Nacional, Instituto Geofísico, Quito, Ecuador, https://orcid.org/0000-0001-6531-6311 (HY)

*Corresponding author: judith.mariniere@univ-grenoble-alpes.fr

Cite this article as Mariniere, J., C. Beauval, J.-M. Nocquet, M. Chlieh, and H. Yepes (2021). Earthquake Recurrence Model for the Colombia–Ecuador Subduction Zone Constrained from Seismic and Geodetic Data, Implication for PSHA, *Bull. Seismol. Soc. Am.* **XX**, 1–21, doi: 10.1785/0120200338

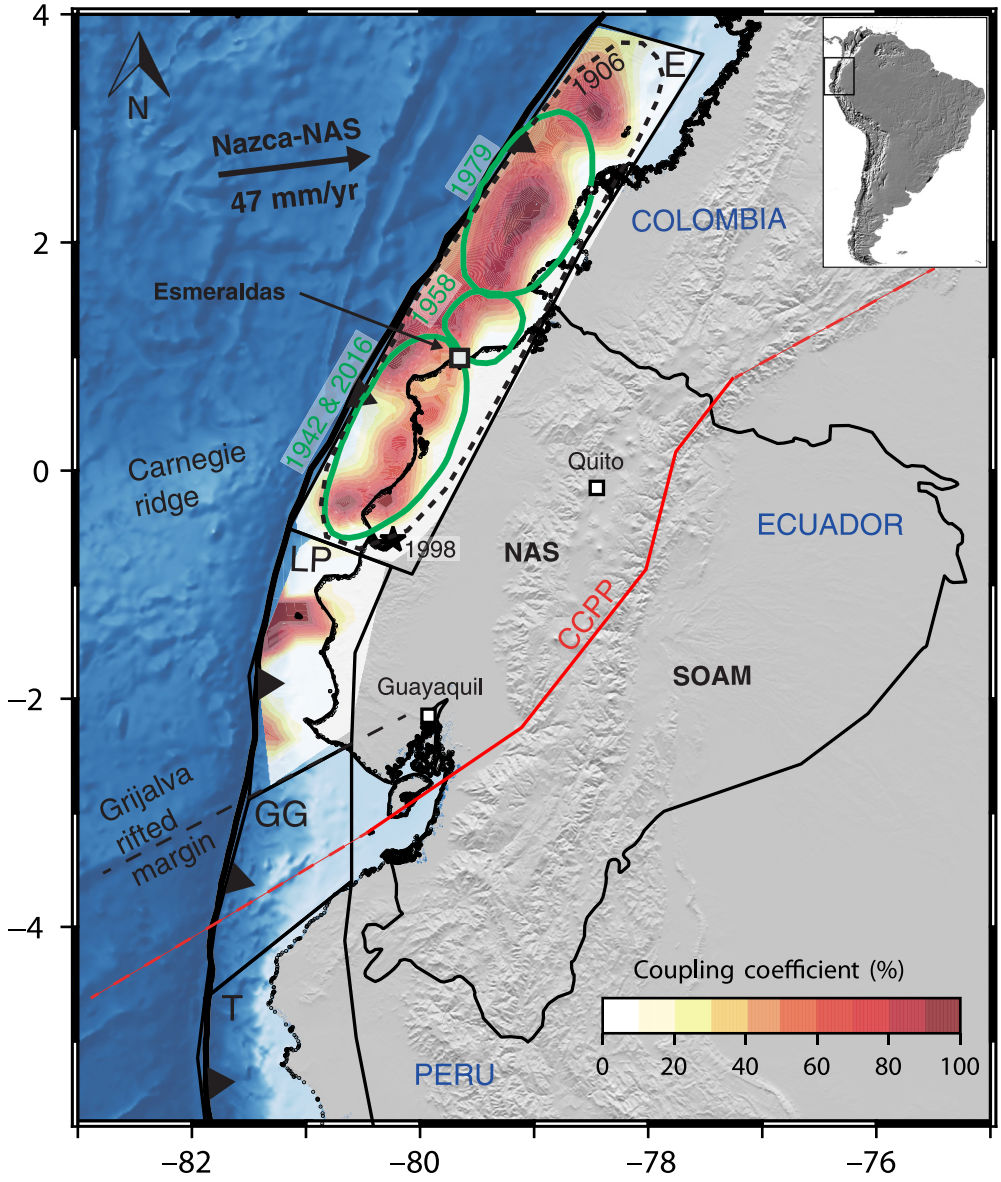

Figure 1. Geodynamic framework of Ecuador and surrounding areas. (Inset) South American continent with the location of the Ecuador framed. The North Andean Sliver (NAS) is bounded to the west by the Nazca subduction trench axis and to the east by the transpressive right-lateral Chingual–Cosanga–Pallatanga–Punà (CCPP) fault system (Alvarado *et al.*, 2016). The CCPP is the main boundary between the NAS and the South America plate (SOAM). The relative convergence rate between the Nazca plate and the NAS increases northward from 46 mm/yr in southern Ecuador to 50 mm/yr in central Colombia. The subduction interface fault segments defined by Yepes *et al.* (2016) and updated in Beauval *et al.* (2018) are reported from north to south: Esmeraldas (E), La Plata (LP), Guayaquil Gulf (GG), and Talara (T). The interseismic coupling model from Nocquet *et al.* (2014) is displayed as well as the, approximate, rupture areas of the 1942 (M_w 7.8), 1958 (M_w 7.6), 1979 (M_w 8.1), and 2016 (M_w 7.8) megathrust events. The rupture area of the 1906 $M_s \sim 8.6$ event corresponds, approximately, to the Esmeraldas segment (see Yepes *et al.*, 2016). The epicenter of the 1998 M_w 7.1 interface event is also displayed (International Seismological Centre–Global Earthquake Model [ISC-GEM] catalog, Di Giacomo *et al.*, 2015). The color version of this figure is available only in the electronic edition.

The present study aims at improving probabilistic seismic hazard assessment (PSHA) in Ecuador. It focuses on the hazard produced by subduction interface earthquakes, occurring along the Esmeraldas segment, as defined in Yepes *et al.* (2016) and updated in Beauval *et al.* (2018). The Esmeraldas segment is ~600 km long, extends from north of the Grijalva-rifted margin to southern Colombia (Fig. 1), and encompasses all rupture areas of the 1906–2016 megathrust earthquake sequence (e.g., Chlieh *et al.*, 2014). Global Positioning System (GPS) data indicate that this segment is, presently, highly coupled (Chlieh *et al.*, 2014; Nocquet *et al.*, 2014). According to Beauval *et al.* (2018), the highest hazard levels are found for sites located on the northern coast, with mean PGA values exceeding 0.6*g* at 475 yr return period for the sites closest to the subduction interface (generic rock site).

The earthquake recurrence model plays a key role in the determination of hazard levels, because it defines the magnitude range to expect for future earthquakes, with associated frequencies. Different models can be implemented to account for interface events. Gutenberg–Richter models can be derived from the available earthquake catalogs (e.g., Medina *et al.*, 2017; Beauval *et al.*, 2018; Petersen *et al.*, 2018a); characteristic models can also be developed with characteristic earthquake recurrence times inferred from the subduction slab convergence rates (e.g., Stirling *et al.*, 2012; Pagani, Johnson, *et al.*, 2020). In the seismic hazard model published by Beauval *et al.* (2018), the authors determined the Gutenberg–Richter recurrence parameters from the well-constrained observed seismic rates in the moderate magnitude range, and they extrapolated these rates up to the maximum magnitudes. Unlike the crustal fault model, Beauval *et al.* (2018) did not use geodetic information to derive earthquake frequencies. The Esmeraldas segment is well

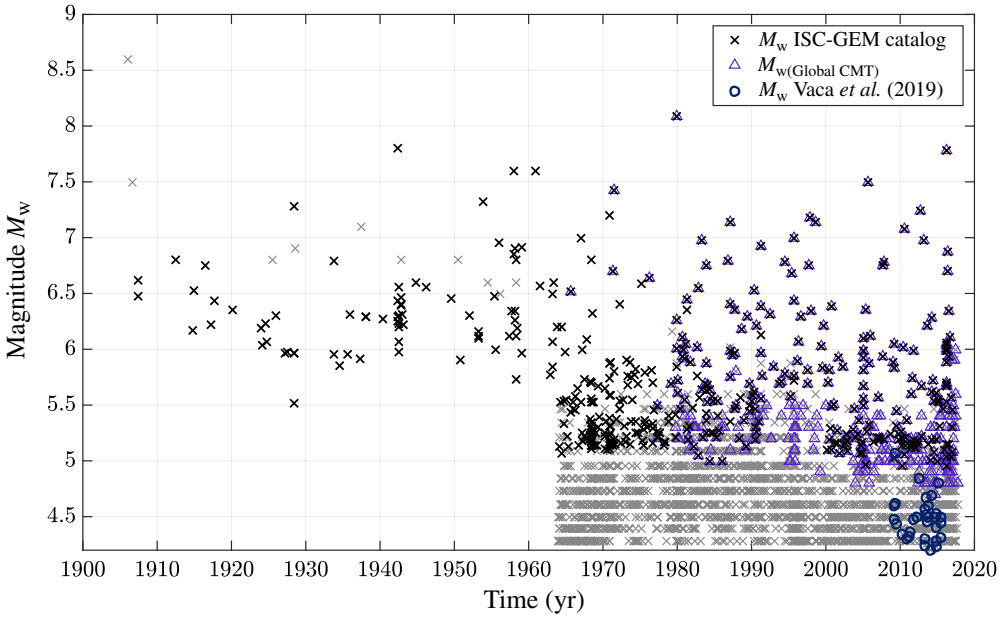

Figure 2. Earthquake catalog for Ecuador (longitudes −82° to −74° and latitudes −7° to 4°), built within this study, covering the time window 1906–2017. The ISC-GEM catalog provides the most authoritative solutions (black crosses); a large part of moment magnitudes in the ISC-GEM catalog are Global Centroid Moment Tensor (Global CMT) magnitudes (triangles). For events that are not in the ISC-GEM catalog, we use the solutions from the ISC event catalog (grey crosses); some of these events also have a Global CMT moment magnitude (triangles), and the other events are described by an m_b magnitude converted into M_w, using the Lolli *et al.* (2014) equations. The moment magnitude earthquake catalog from Vaca *et al.* (2019) is included (circles). Details are provided in the An Earthquake Catalog for Seismic Hazard Assessment in Ecuador section in Appendix. The color version of this figure is available only in the electronic edition.

instrumented with GPS stations at distances less than 100 km from the trench axis, and high-resolution models of interseismic coupling are available (Chlieh *et al.*, 2014; Nocquet *et al.*, 2014; Gombert *et al.*, 2018). Our aim here is to combine seismic and geodetic data, to constrain earthquake recurrence models for the ~600 km long subduction interface that extends from northern Ecuador to central Colombia. Because the quantification of uncertainties is a key aspect in PSHA studies, we identify uncertainties related to both the seismic and the geodetic data, and propagate these uncertainties up to the hazard results.

EARTHQUAKE RECURRENCE MODELS AND INTERSEISMIC COUPLING MODELS

A seismic catalog extending over 112 yr

In Ecuador, the earliest events reported in the historical macroseismic catalog date back to the middle of the sixteenth century (Egred, 2009), a few years after the arrival of the Spaniards. Until the end of the nineteenth century, the historical information mostly describes effects of earthquakes inland, in the Cordillera (see, e.g., Beauval *et al.*, 2013). The first coastal earthquake for which several are reported is the 1896 event; however, the dataset is too sparse to infer a reliable location and magnitude for this event (Keller, 2014). Therefore, the earthquake catalog for the subduction interface extends at the maximum over 112 yr and includes early-instrumental and instrumental events. Nonetheless, marine paleoseismology studies are undergoing at the Ecuadorian margin (Proust *et al.*, 2016; Migeon *et al.*, 2017). For now, they have identified turbidites dated, approximately, 600 yr ago, which could have been triggered by an event equivalent to the great 1906 subduction earthquake (Migeon *et al.*, 2017).

We build an earthquake catalog for the area, making use of global catalogs (Fig. 2, Table A1). We decide not to include local catalogs, to ensure a certain level of homogeneity in moment magnitude. As a consequence, the minimum magnitude of completeness is quite high ($M_w \sim 4.8$ since 1964). Solutions in the ISC-GEM catalog (version 7.0 [v.7.0]) are considered the most authoritative. All ISC-GEM hypocenter locations were computed with the same algorithm and velocity model (Storchak *et al.*, 2015); events are described by either a published moment magnitude, M_w from the Global CMT catalog (Ekström *et al.*, 2012), or a proxy M_w value inferred from an M_s or m_b magnitude (Di Giacomo *et al.*, 2015). For earthquakes that are not in the ISC-GEM catalog, we use solutions from the ISC event catalog (Storchak *et al.*, 2017; ISC, 2020) over its reviewed period. In this case, M_w is either retrieved from the Global CMT catalog or obtained from ISC m_b and M_s magnitudes, using the global conversion equations from Lolli *et al.* (2014). The exact selection scheme followed for building the catalog is detailed in the An Earthquake Catalog for Seismic Hazard Assessment in Ecuador section in Appendix.

Earthquakes that may be associated with the Esmeraldas interface segment are displayed in Figure 3. All events falling inside the segment with hypocentral depths between 0 and 50 km are considered (Yepes *et al.*, 2016). Since 1900, the area has been very active, experiencing six earthquakes with magnitudes M_w between 7.1 and ~8.6, and 38 events with magnitudes between 6.0 and 7.0. To estimate seismic rates representative of long-term seismicity, it is current practice in probabilistic seismic hazard studies to decluster the earthquake catalog (e.g., Teng and Baker, 2019). The strong aftershock sequences can bias the estimation of the rates and the *b*-value, characterizing the exponential decrease of the number of events with respect to

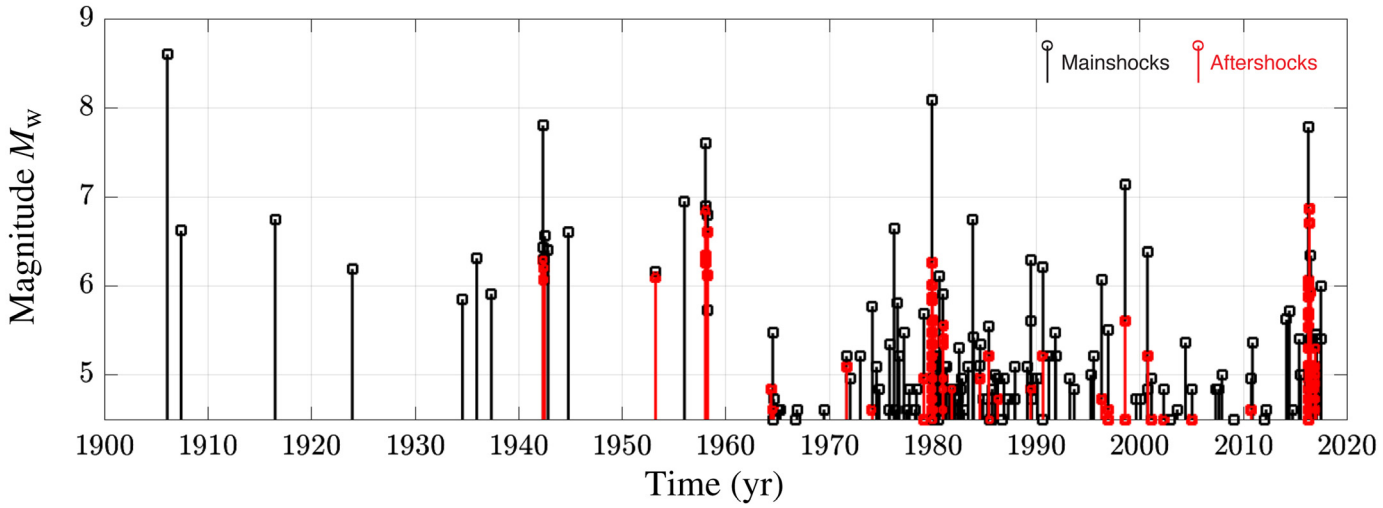

Figure 3. Magnitude versus time, catalog homogenized in M_w (this study, $M_w \geq 4.5$) in the Esmeraldas interface source zone (shown in Fig. 1). Black represents mainshocks, and red represents clustered events, as identified by the Reasenberg algorithm. Before 1964, the catalog only includes earthquakes with $M_w > 5.5$. The aftershock sequence following the 1979 $M_{w(GlobalCMT)} = 8.1$ event and of the 2016 $M_{w(GlobalCMT)} = 7.8$ represents 38% and 31%, respectively, of all clustered events in the zone. The color version of this figure is available only in the electronic edition.

magnitude. We apply the Reasenberg (1985) declustering algorithm, with parameters indicated in Table A2 (the An Earthquake Catalog for Seismic Hazard Assessment in Ecuador section in Appendix). We use Reasenberg (1985) algorithm rather than Gardner and Knopoff (1974), because it is more adapted to large interface earthquakes (The linking algorithm enables to identify aftershocks along the entire rupture plane.). In the Esmeraldas source zone, 52% of the $M_w \geq 4.5$ events are identified as clustered events (155 out of 297 events). Two-thirds of these clustered events belong to the aftershock sequences of the 1979 and 2016 megathrust earthquakes (Fig. 3). However, in terms of seismic moment rate, these clustered events represent only 0.8% of the moment rate calculated over the whole catalog.

In the depth range considered, not all events are related to the interface, some might be related to crustal shallow faults. Given the large uncertainties on the depth solutions, discriminating between interface and crustal events based on the hypocentral locations is elusive. For most earthquakes with a magnitude $M_w \geq 5.0$–5.2 after 1979, the Global CMT catalog provides a solution (Fig. 2), including the focal mechanism. We apply some simple criteria, that is, a rake within the range 30°–150° and a dip lower than 45°, to select earthquakes that might correspond to reverse or reverse-oblique faulting at the plate interface (see fig. 4.18 in Pacific Earthquake Engineering Research Center [PEER] Report, 2020, which displays the distribution of rake and dip angles for interface events in the Next Generation Attenuation Subduction database). We find that within the Esmeraldas source zone limits, 88% of the earthquakes in the Global CMT catalog fall in this category. About 12% of events might be related to crustal shallow faults. Observed seismic rates estimated from the newly built catalog will be corrected accordingly.

Modeling earthquake recurrence

The Weichert (1980) maximum-likelihood method allows to determine the Gutenberg–Richter recurrence parameters from magnitude intervals with varying time windows of completeness (productivity a and exponential coefficient b, Gutenberg and Richter, 1944). The catalog is considered to be complete for $M_w \geq 6.6$, in the early instrumental period from 1900 to 1920, for $M_w \geq 6.0$ in the period from 1920 to 1950, for $M_w \geq 5.7$ in the period from 1950 to 1964, and for $M_w \geq 4.8$ from 1964 (Table A3, 0.3 magnitude bin width used). Applying the Weichert method over the magnitude range with populated bins, that is, between M_w 4.5 and 7.2, we obtain from the declustered earthquake catalog a b-value of 0.62 ± 0.05 (with an a-value 3.06; Fig. 4a). Seismic rates for larger magnitudes ($M_w > 7.2$) are not meaningful, because they are calculated from one or two occurrences. Although debated (Ye *et al.*, 2016; Gombert *et al.*, 2018), the occurrence rate of large subduction earthquakes, since 1906, has been proposed to be abnormally high and being part of an earthquake supercycle (Nocquet *et al.*, 2017). In any case, the observation time window is too short to estimate the long-term average recurrence time of these large events. Because there is no trace in the historical archives of a large megathrust earthquake that would have hit the coast during the seventeenth, eighteenth, and nineteenth centuries (Egred, 2009; Beauval *et al.*, 2013), the rates of events $M_w > 7.2$ could also be calculated, extending the time window to 400 yr (resulting in orange dots in Fig. 4b). Alternatively, we can obtain these rates by extrapolating the model established from the moderate-magnitude range to the upper-magnitude range, but, again, there is no unique way to proceed. Different forms have been proposed in the literature for modeling the rates close to the maximum

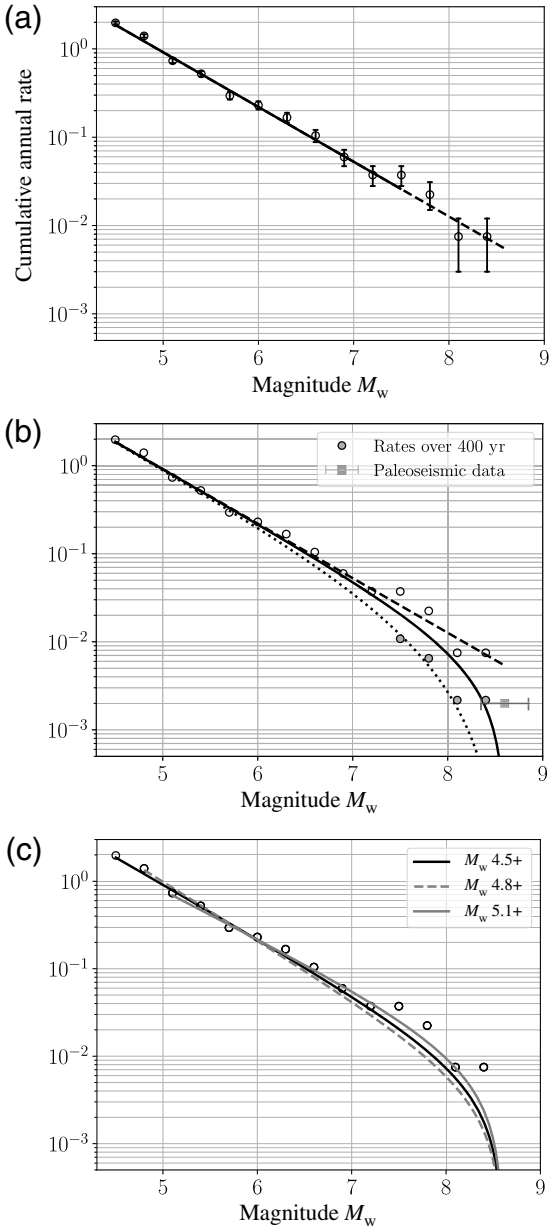

Figure 4. Magnitude–frequency distributions for Esmeraldas interface source zone (Fig. 1); (a,b) recurrence parameters determined over the moment magnitude range $M_w = 4.5$–7.2 ($a = 3.06$, $b = 0.62$). (a) The recurrence model (solid line) is superimposed to observed rates; error bars indicate the uncertainty on the rates assuming a Poisson model (5th and 95th percentiles); model is extrapolated (dashed line) up to the maximum observed magnitude ($M_s8.6 \pm 0.25$, Ye *et al.*, 2016). (b) Three different forms are used to extrapolate the model in the upper-magnitude range (Anderson and Luco, 1983): Form 1 (dashed line), Form 2 (solid line), and Form 3 (dotted line); orange dots represent rates for $M_w \geq 7.5$ calculated over 400 yr, rather than 112 yr; at least one earthquake equivalent to the 1906 event every 600 yr, according to Migeon *et al.* (2017) paleoseismic study (green square). (c) Uncertainty on the modeling of the recurrence from the earthquake catalog: three (a,b) pairs inferred from the magnitude intervals 4.5–7.2 ($a = 3.06$, $b = 0.62 \pm 0.05$, black), 4.8–7.2 ($a = 3.35$, $b = 0.67 \pm 0.06$, gray-dashed line), and 5.1–7.2 ($a = 2.65$, $b = 0.55 \pm 0.08$, gray solid line). The color version of this figure is available only in the electronic edition.

magnitude. The selection of one model over the other remains arbitrary, because the data in the upper-magnitude range are always too sparse to discriminate between the different proposed forms (Zöller, 2013).

Here, we consider the three alternative Gutenberg–Richter recurrence models proposed by Anderson and Luco (1983), which have been used in many subsequent studies. All models are truncated at the maximum magnitude M_{max}, but the three forms of recurrence models forecast different rates in the upper-magnitude range ($M_w > 7.0$, Fig. 4b). The maximum observed magnitude in the Esmeraldas source zone is the 1906 earthquakes, with $M_s8.6 \pm 0.25$ as estimated by Ye *et al.* (2016); the M_{max} bounding the recurrence model must be larger or equal to this observed magnitude. The total number of earthquakes above a given magnitude can be estimated as follows, depending on the form selected:

$$N(m) = 10^{a-bm} \quad \text{for } m \leq M_{max}, \qquad (1,\ \text{Form 1})$$

$$N(m) = 10^{a-bm} - 10^{a-bM_{max}} \quad \text{for } m \leq M_{max}, \qquad (2,\ \text{Form 2})$$

$$N(m) = 10^{a-bm} - 10^{a-bM_{max}} - b\ln(10)(M_{max} - m)10^{a-bM_{max}} \quad \text{for } m \leq M_{max}. \qquad (3,\ \text{Form 3})$$

The corresponding discrete noncumulative rates can be found in the Discrete Noncumulative Rates for Gutenberg–Richter Forms 1–3 section in Appendix. Form 1 has similarities with the Youngs and Coppersmith (1985) characteristic earthquake model, with rates for the last magnitude bin larger than predicted by the moderate-to-large magnitude range (Fig. A1). Forms 2 and 3 predict fewer large magnitude earthquakes than Form 1. Form 2 is the most prevalent in PSHA studies (e.g., Beauval *et al.*, 2014; Mihaljević *et al.*, 2017; Grünthal *et al.*, 2018). It is the form implemented in OpenQuake (Pagani *et al.*, 2014, "Truncated Gutenberg–Richter MFD"). Form 1 has been less used in PSHA, but it is quite common in the literature comparing seismic moment accumulation from geodesy and moment released by earthquakes (e.g., D'Agostino, 2014; Avouac, 2015; Stevens and Avouac, 2016, 2017).

As in every seismic hazard study, the earthquake catalog and the seismic rates estimated bear significant uncertainties (see, e.g., Beauval and Scotti, 2003; Beauval *et al.*, 2013, 2018, 2020; Brax *et al.*, 2019). There are uncertainties on the selection of the best magnitudes and locations from available solutions, on the choice of the magnitude conversion equations, on the determination of time windows of completeness, and on the cutoff magnitude used to model the recurrence. Here, we consider the uncertainty related to the cutoff magnitude and use successively the minimum magnitudes of 4.5, 4.8, and 5.1. Three alternative a and b pairs are derived (Fig. 4c, b-values 0.62 ± 0.05,

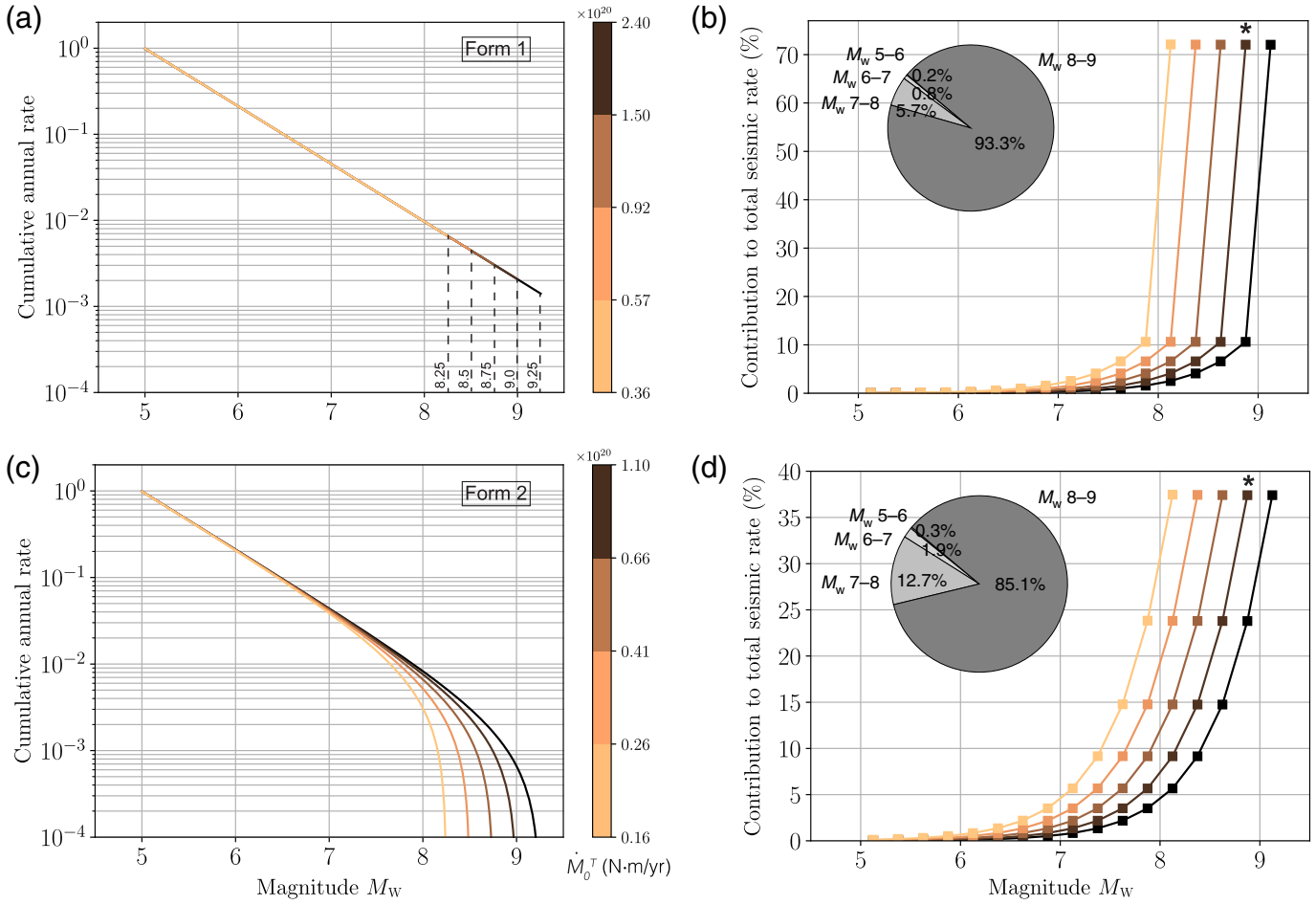

Figure 5. Implication of a Gutenberg–Richter earthquake recurrence model in terms of seismic moment rate, exercise with a model based on the *a*- and *b*-values calculated for the Esmeraldas source zone ($a = 3.35$, $b = 0.67$). (a, c) Impact of M_{max} on the total seismic moment rate (color bar) with M_{max} arbitrarily varying from 8.25 to 9.25 with a 0.25 step. (b,d) Contribution of each magnitude bin to the total seismic moment rate, in percentage. The pie charts display the contribution per 1° magnitude interval for the recurrence model with M_{max} 9.0 (indicated with a star). The total seismic moment rate is calculated with Form 1 according to: $\dot{M}_0^T = \frac{c}{c-b} 10^{a+d+(c-b)M_{max}}$, and with Form 2 according to: $\dot{M}_0^T = \frac{b}{c-b} 10^{a+d+(c-b)M_{max}}$. Contribution of each magnitude bin to the total seismic moment rate calculated according to: $\frac{1}{\dot{M}_0^T} \int_m^{m+0.25} \lambda(m) 10^{cm+d} dm$, with $\lambda(m)$ the annual seismic rate, $c = 1.5$ and $d = 9.1$, the coefficient to estimate seismic moment from the moment magnitude (e.g., Appendix, M_{max} ensuring a moment-balanced earthquake recurrence model). The color version of this figure is available only in the electronic edition.

0.67 ± 0.06, and 0.55 ± 0.08). In the Weichert method, the magnitude bins that are the most populated control the parameter estimation. The model based on a magnitude cutoff 4.5 predicts fewer events with $M_w \geq 6.3$ than observed over the past 112 yr; the model based on a magnitude cutoff 5.1 predicts, approximately, the rates observed up to magnitude 7.2 (Fig. 4c). The *b*-values obtained are rather low, but they are within the range of *b*-values found in the literature for subduction interface segments. For instance, Medina *et al.* (2017) found *b*-values around ~0.75 for the interface source zones in Chile. Marzocchi *et al.* (2016) analyzed the frequency–magnitude distribution of the interface earthquakes at different subduction zones worldwide; the *b*-values found vary between 0.62 and 2. In a study focused on the Nazca subduction zone, Pagani, Johnson, *et al.* (2020) evaluated *b*-values between 0.64 and 1.11, depending on the interface segment of the South American subduction zone. They obtained a *b*-value of 0.64 for their ~850 km segment extending from −1.0° to 5.5° latitude—a segment that encompasses the Esmeraldas segment.

The upper-magnitude range controls the seismic moment budget

Using a Gutenberg–Richter model with parameters determined for the Esmeraldas zone, we now show how the seismic moment budget varies with the form selected and the magnitude range considered (Fig. 5). An increase of 0.2 in magnitude degree corresponds to a twofold increase in the corresponding seismic moment M_0 (Hanks and Kanamori, 1979):

$$M_0 = 10^{cM_w+d}(\mathrm{N \cdot m}) \quad \text{with} \quad c = 1.5 \quad \text{and} \quad d = 9.1. \quad (4)$$

Figure 5 displays Gutenberg–Richter models with increasing maximum magnitudes (Form 1 in Fig. 5a and Form 2 in

Fig. 5c), together with the corresponding total seismic moment rate (obtained by integrating the model over the whole magnitude range). We calculate the contribution to the total seismic moment rate per magnitude bin, using a bin width of 0.25 (Fig. 5b,d). We show that the exponential decrease of the seismic rates with increasing magnitude (Fig. 5a,c) is counterbalanced by the exponential increase of the seismic moment. Considering Form 1 and a *b*-value of 0.67 (Fig. 5b), the upper 1° magnitude interval, that is, $[M_{max} - 1M_{max}]$, contributes to ~93% of the total seismic moment rate. Considering Form 2 (Fig. 5c,d), the upper 1° magnitude interval contributes to ~85% of the total seismic moment rate. With an M_{max} equal to 9.0, the contribution of events with magnitudes lower than 7 is around 2%.

The 112 yr long earthquake catalog helps to constrain the moderate magnitude range but is useless to discriminate between forms close to M_{max}. Geodetic measurements provide an estimate of the rate of moment deficit accumulating on the subduction interface. Such information can be used to define the overall budget expected to be released in earthquakes. By combining this geodetic information with the information from the catalog in the moderate magnitude range, the rates in the upper-magnitude range can be fully constrained.

Interseismic models available for the Ecuadorian subduction interface

Compared with other subduction segments, the Esmeraldas interface source zone benefits from relatively well-constrained interseismic coupling models. Indeed, a coastline–trench distance usually shorter than 80 km, with several peninsulas, combined with a shallow-dipping interface, allows a precise determination of the coupling at depth greater than 10 km of the megathrust interface (Chlieh *et al.*, 2014). The GPS network has an average density of measurement sites every 70 km or less. Long-time series dating back to the 1990s for campaign sites and 2008 for continuous GPS are available. Several interseismic coupling models have been proposed for Ecuador and the southern Colombia subduction zone (Chlieh *et al.*, 2014; Nocquet *et al.*, 2014; Gombert *et al.*, 2018; Staller *et al.*, 2018; Sagaiya and Mora-Páez, 2020). Here, we extend the existing coupling models from Chlieh *et al.* (2014) and Nocquet *et al.* (2014) up to latitude 4° N in central Colombia (Fig. 6). Both approaches use a backslip approach (Savage, 1983) and invert the interseismic velocity field in a NAS reference frame. The uncertainties of their models are, principally, due to the limited spatial resolution of GPS data at less than 50 km of the trench axis (corresponding to the very 0–20 km shallowest portion of the megathrust interface).

Nocquet *et al.* (2014) discretized the subduction interface fault into 1024 quasiequilateral triangles, each having an average edge length of 30 km, following the Slab 1.0 (Hayes *et al.*, 2012) geometry subduction interface. The inversion follows a linear Bayesian formulation (Tarantola, 2005) modified to account for nonnegative constraints (Nocquet, 2018). This technique enables to explore the range of possible models, by varying the a priori model (from null to fully coupled plate interface) as well as the damping and the smoothing parameters (through a model covariance matrix). From the range of acceptable interseismic models obtained (weighted root mean square [wrms] ≤1.1 mm/yr), we select three models representatives of the uncertainties (Fig. 6a–c): the minimum, the best estimate, and the maximum model.

Chlieh *et al.* (2014) applied a nonlinear inversion of the GPS data, based on a stochastic simulated annealing algorithm (Chlieh *et al.*, 2011). They divided the megathrust interface into 20 km diameter point-source elements, following the slab geometry. Local geologic and seismic data are used to establish the slab (Graindorge *et al.*, 2004; Gailler *et al.*, 2007; Hayes *et al.*, 2012; Font *et al.*, 2013). They used the local average slip vector direction from the Global CMT catalog and the relative Nazca–NAS long-term plate rate, to constrain the backslip direction to ±10° with respect to the Nazca–NAS predicted value. The acceptable range of models has a smoothing factor between 0.1 and 1.0 and a wrms ≤1.1 mm/yr. From these ranges of interseismic models, we select three models representatives of the uncertainties (Fig. 6d–f): the minimum, the best estimate, and the maximum model.

The comparison of the models obtained by Chlieh *et al.* (2014) and Nocquet *et al.* (2014) indicates some differences in the spatial distribution of the highly coupled areas over the megathrust interface, but the range of moment deficit rate estimated is quite similar in both approaches. All models show that the coupling is principally restricted above the 40 km depth of the slab interface with a highly heterogeneous coupling distribution along the Esmeraldas segment, and an ~200 km long locked area at the center of the zone (at latitude of 2° N), connecting to smaller locked patches to the north and to the south. Three major asperities are distinguishable in rougher models. The rupture areas of the megathrust events, 1906 (M_s ~ 8.6, Ye *et al.*, 2016), 1942 ($M_{w(ISC-GEM)}$ 7.8), 1958 ($M_{w(ISC-GEM)}$ 7.6), 1979 ($M_{w(GlobalCMT)}$ 8.1), and 2016 ($M_{w(GlobalCMT)}$ 7.8), correlate well with regions of high interseismic coupling (Fig. 1). The interseismic coupling for the whole Esmeraldas source zone is around 40%–42%, if taken as an average from the trench down to 50 km depth. For the hazard study, we keep three values to represent the uncertainty on the coupling: the minimum value of all models, the average of the best-estimate models, and the maximum value of all models.

COMBINING SEISMIC AND GEODETIC INFORMATION: MOMENT-BALANCED EARTHQUAKE RECURRENCE MODELS

Moment conservation principle

The general idea of moment conservation was introduced more than 40 yr ago (Brune, 1968; Anderson, 1979; Molnar, 1979). Anderson (1979) suggested to use geological slip rates on faults to estimate seismic moment release and derive

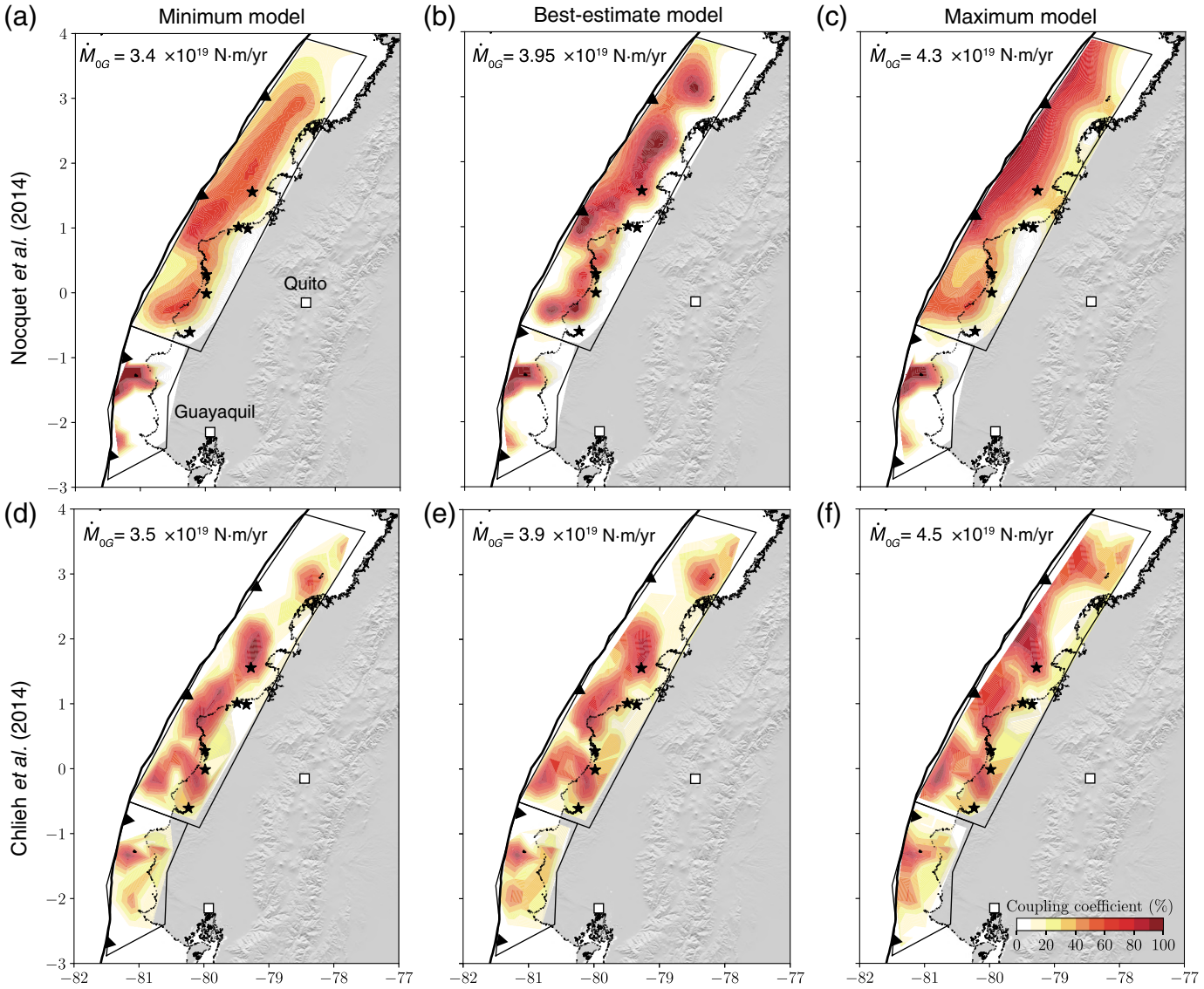

Figure 6. Interseismic coupling (ISC) maps. ISC quantifies the degree of locking of the subduction interface zone. (a–c) ISC models from Nocquet *et al.* (2014) (the minimum, the best-estimate, and the maximum ISC models). (d–f) ISC models from Chlieh *et al.* (2014) (the minimum, the best-estimate, and the maximum ISC models). A coupling coefficient (χ_i) equal to 100% corresponds to a fully locked fault patch, whereas a coupling coefficient equal to 0% corresponds to a patch creeping at the long-term slip rate. χ_i is defined as the ratio between the slip deficit and the long-term slip rate. Black stars represent epicenters of megathrust events $M_w > 7.0$ in the ISC-GEM catalog (Di Giacomo *et al.*, 2015). The value of moment deficit rate (top left) is calculated over the Esmeraldas interface with $\mu = 30$ GPa. The color version of this figure is available only in the electronic edition.

earthquake recurrence models. Anderson and Luco (1983) discussed how the slip-rate constraints can be used either to estimate M_{max} from the occurrence rates of small magnitude earthquakes or to estimate occurrence rates when M_{max} is already known, for example, from scaling relationships. In an article focused on southern California, Ward (1994) showed how seismological, geodetic, and geological data can be combined to establish a recurrence model that forecasts earthquake frequencies for seismic hazard assessment. For the same region, Field *et al.* (1999) developed earthquake recurrence models matching the observed rates and consistent with the conservation of seismic moment rate. They demonstrated that some parameters, such as the *b*-value, the choice of the magnitude–frequency distribution, or the exact moment-magnitude definition used, can have a non-negligible impact on the seismic rates and the maximum magnitude. More recently, Kagan and Jackson (2013) and Rong *et al.* (2014) applied the moment conservation principle in subduction zones to estimate the maximum magnitudes, again by matching the geodetic deformation rate to that predicted by earthquakes with a magnitude–frequency distribution. Finally, in a review article analyzing the partitioning between seismic and aseismic fault slip in areas where interseismic coupling maps are available, Avouac (2015) revisited this concept discussing the maximum magnitude earthquake required for the closure of the slip budget over the long term.

In these publications, the Gutenberg–Richter model used varies, and usually only one model is employed. A large part of the literature uses Form 2 in Anderson and Luco (1983) (e.g., Ward, 1994; Field *et al.*, 1999; Hyndman *et al.*, 2003; Mazzotti *et al.*, 2011). Some authors use Form 1 (e.g., Avouac, 2015; Michel *et al.*, 2018; Stevens *et al.*, 2018), whereas others (e.g., Kagan and Jackson, 2013; Rong *et al.*, 2014) employ the "tapered Gutenberg–Richter distribution" introduced by Kagan (2002)—a model that we do not consider here. We found only one study by Pancha *et al.* (2006) that tested several forms for extrapolating the recurrence model up to $M_{\max}$.

Determining $M_{\max}$ so that the recurrence model is moment balanced

For subduction megathrust earthquakes in Ecuador and southern Colombia, we propose to derive recurrence models by anchoring the recurrence curve to the observed seismic rates in the moderate-magnitude range (up to $M_w \sim 7.0$), then extrapolating this model to the upper-magnitude range, and bounding the model with an $M_{\max}$ value, ensuring that it is moment balanced. Moment balanced means that the rate of seismic moment accumulation estimated from geodesy is accommodated by the Gutenberg–Richter model (e.g., Petersen *et al.*, 2008). Our strategy is to obtain a distribution for potential $M_{\max}$ values, accounting for uncertainties on the observed seismic rates and on the form of the curve close to $M_{\max}$, as well as on the estimation of the seismic moment budget. By anchoring the model to seismic rates estimated over the past 112 yr, we assume that the Gutenberg–Richter model is stable in time, and that past seismicity is representative of future seismicity in this magnitude range.

From the moment deficit rate accumulating in the interseismic period, and assuming that a fraction of it is released through aseismic transient slip, the moment rate released in earthquakes can be estimated (Avouac, 2015). In this region, the interseismic strain models are inferred from GPS measurements mostly collected over the past 20 yr. We need to assume that the loading rate estimated over that period is representative of the long-term interseismic rate. The rate of moment deficit derived from interseismic geodetic measurements and accumulating on the plate interface can be written as

$$\dot{M}_{0G} = \int_{\text{megathrust}} \mu S \chi_i ds, \tag{5}$$

in which μ is the shear modulus, S the long-term relative plate convergence rate, and χ_i the interseismic coupling. The interseismic coupling χ_i is the ratio of the deficit of slip rate in the interseismic period to the long-term slip rate. It quantifies the degree of locking of the slab; $\chi_i = 1$ corresponds to a locked patch, $\chi_i = 0$ to a patch fully creeping at the plate convergence rate. The moment deficit rate obtained is in $\mathrm{N \cdot m/yr}$. The relative Nazca–NAS convergent rate S, along the Esmeraldas subduction interface, is around 47 mm/yr (Nocquet *et al.*, 2014).

In the long term, the moment deficit rate $\dot{M}_{0G}$ (equation 5) is, on average, equal to the moment rate released by earthquakes and aseismic transients (i.e., afterslip following large earthquakes and episodic slow-slip events [SSEs]). Following Avouac (2015), let α be the fraction of slip deficit that will be released in earthquakes. The earthquake recurrence model is moment balanced, if its corresponding cumulative annual seismic moment rate equals the fraction of moment deficit that is released seismically $\alpha \dot{M}_{0G}$. The equation to solve, in the case of Form 2 (equation 2), is:

$$\int_{-\infty}^{M_{\max}} b \ln(10) 10^{cm+d} 10^{a-bm} dm = \alpha \dot{M}_{0G}, \tag{6}$$

with parameters c and d from the moment-magnitude definition (equation 4 and Appendix, $M_{\max}$ ensuring a moment-balanced earthquake recurrence model), and Gutenberg–Richter a and b determined from observed rates on the moderate-magnitude range (the Modeling Seismic and Geodetic Data section). Hence, the maximum magnitude bounding the recurrence model can be determined as follows (see Appendix, $M_{\max}$ ensuring a moment-balanced earthquake recurrence model):

$$M_{\max} = \frac{1}{c-b}\left(\log_{10}(\alpha \dot{M}_{0G}) - \log_{10}\left(\frac{c}{c-b}\right) - a - d\right), \tag{7, Form 1}$$

$$M_{\max} = \frac{1}{c-b}\left(\log_{10}(\alpha \dot{M}_{0G}) - \log_{10}\left(\frac{b}{c-b}\right) - a - d\right), \tag{8, Form 2}$$

$$M_{\max} = \frac{1}{c-b}\left(\log_{10}(\alpha \dot{M}_{0G}) - \log_{10}\left(\frac{b^2}{c(c-b)}\right) - a - d\right). \tag{9, Form 3}$$

Figure 7a displays different recurrence models having the same recurrence parameters a and b, and, the same moment deficit rate$\dot{M}_{OG}$, considering Form 2. We show how varying the value of α impacts the maximum magnitude, meaning that the knowledge of aseismic slip is fundamental to assess seismic hazard. Considering that all the deformation measured is released in earthquakes (i.e., $\alpha = 1$) leads to the maximum magnitude of 8.7. Considering that only 50% of the deformation is released in earthquakes (i.e., $\alpha = 0.5$) leads to a model bounded at magnitude 8.4, a value lower than the great 1906 event, suggesting that $\alpha > 0.5$. The assumption on α impacts the recurrence model obtained. The uncertainty on the

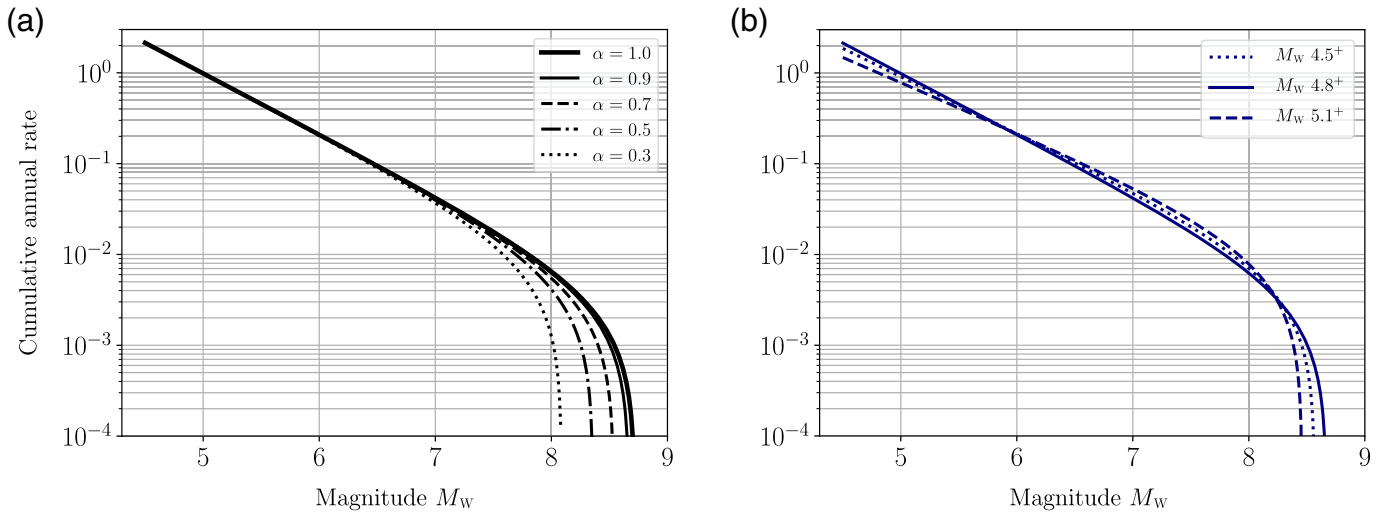

Figure 7. Moment-balanced earthquake recurrence models for Esmeraldas source zone, exercise to illustrate the influence of input parameters uncertainties. All models correspond to a constant moment deficit rate ($\dot{M}_O = 3.92 \times 10^{19}$ N · m/yr). (a) Recurrence parameters are fixed ($a = 3.35$, $b = 0.67$), the smaller the α-value, the lower the resulting maximum magnitude M_{max}. (b) α is fixed to 0.9; three alternative a and b pairs are tested (see Fig. 4c); the larger the a- and b-values, the larger the resulting maximum magnitude. The color version of this figure is available only in the electronic edition.

recurrence parameters a and b may also impact the recurrence model (Fig. 4c). Keeping the moment deficit rate $\dot{M}_{OG}$ and α fixed, considering slightly lower a- and b-values, the M_{max} value decreases (Fig. 7b), whereas slightly larger a- and b-values require a larger M_{max} value.

MOMENT-BALANCED RECURRENCE MODELS FOR ESMERALDAS INTERFACE AND ASSOCIATED HAZARD LEVELS

A set of moment-balanced recurrence models accounting for uncertainties

We apply the methodology to the Esmeraldas interface source zone, modeled as a single plane dipping with 20° between the trench and 50 km depth. We use the same interface segmentation as in Beauval *et al.* (2018). The Esmeraldas segment corresponds approximately to the rupture area of the 1906 earthquake ($M_s \sim 8.6$, Ye *et al.*, 2016). The southern limit has been defined as the southern end of the 2016 M_w 7.8 rupture area and overlaps with the 1942 M_w 7.8 rupture limit (Ye *et al.*, 2016). The northern boundary was set at ∼4° N at a kink in the Colombian trench azimuth, passing from a northwest–southeast trend to the south to, approximately, north–south to the north; it also corresponds to a difference in seafloor ages. The reader is referred to Yepes *et al.* (2016) and Beauval *et al.* (2018), for detailed explanations on the segment limits.

The candidate recurrence models are anchored to the instrumental seismic rates, and their M_{max} values are calculated so that the models are moment balanced with the moment deficit rate inferred from geodesy. We account for uncertainties on the observed seismic rates, on the moment deficit rates, and on the fraction of slip deficit that is seismic. We explore the following uncertainties (Fig. 8):

- There are three pairs of a and b recurrence parameters.
- There are three different forms to extrapolate the recurrence models up to M_{max}.
- There are three moment deficit rate estimates based on the interseismic coupling models available; the best-estimate value is attributed a larger weight (50%) than the minimum and the maximum values (25% each).
- There are three values for the average rigidity modulus used to determine the moment deficit rate: 30, 40, and 50 GPa (e.g., Bilek and Lay, 1999; Scala *et al.*, 2020).
- For α, the fraction of the slip deficit that is released seismically, we include four alternative values (0.3, 0.5, 0.7, and 0.9). This large range of values reflects the important uncertainty on this parameter for the Esmeraldas zone and is made to encompass different possible behaviors. Recurrent SSEs have been commonly observed or inferred north of the 2016 M_w 7.8 Pedernales earthquake rupture area (Mothes *et al.*, 2013; Vaca *et al.*, 2018). However, the lack of SSE moment estimates for events prior to 2013 prevents any moment budget to be determined. For the Pedernales area, Rolandone *et al.* (2018) show that early afterslip released as much as 30% of the coseismic moment during one month following the earthquake, suggesting that α could be lower than 0.7.

The exploration of uncertainties results in 324 different parameter combinations that lead to 324 alternative maximum magnitudes. The distribution of the maximum magnitudes obtained follows roughly a Gaussian distribution centered on $M_{max} \sim 8.4$ (Fig. 9a). By sorting the M_{max} values according to the recurrence model form used, we show that the uncertainty on the choice of the form controls the overall uncertainty

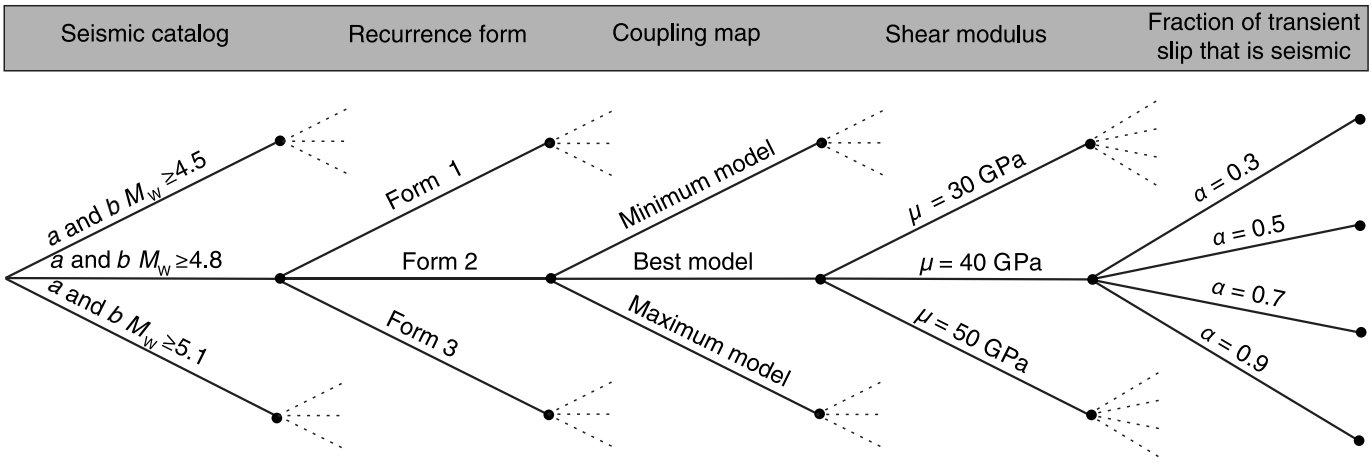

Figure 8. Exploration of uncertainties on the input parameters and propagation up to the final earthquake recurrence model for Esmeraldas interface source zone ($3 \times 3 \times 3 \times 3 \times 4 = 324$ combinations). The shear modulus is expressed in GPa (1 GPa $= 10^9$ N/m^2). The alternative branches are equally weighted, except for the interseismic coupling (the best model is weighted 50%, and the minimum and the maximum models are weighted 25% each).

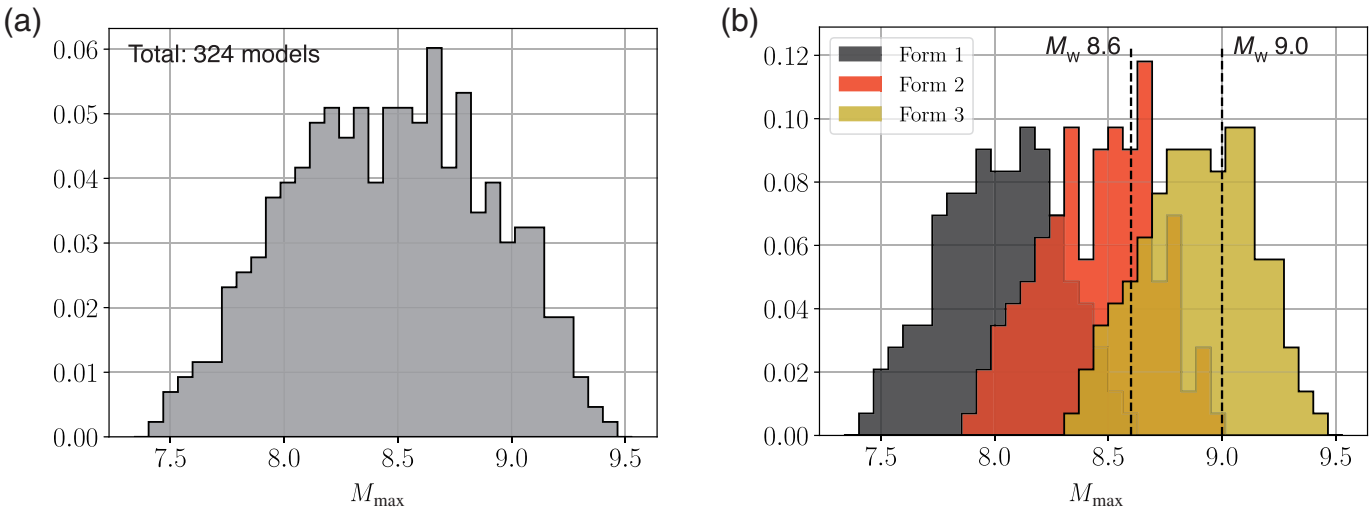

Figure 9. Distribution for the maximum magnitude M_{max} bounding the moment-balanced recurrence models for the Esmeraldas interface source zone. (a) Full distribution that accounts for all uncertainties considered (324 values, Fig. 8). (b) The M_{max} values are sorted depending on the recurrence model form (Form 1 in black, Form 2 in red, and Form 3 in yellow; 108 models per form). We consider that realistic M_{max} values are within the interval 8.6–9.0: the maximum magnitude earthquake must be larger or equal to the 1906 earthquake ($M_w \sim 8.6$) and lower or equal to 9.0, the maximum magnitude inferred from the scaling relationships Strasser *et al.* (2010). The color version of this figure is available only in the electronic edition.

(Fig. 9b). Form 1 leads to M_{max} values lower than Form 2, and Form 2 leads to M_{max} values lower than Form 3. This can be easily understood from Figure 10; for a fixed moment budget, Form 1 predicts larger rates for magnitudes $M_w > 7.5$ than Form 2, and Form 2 larger rates than Form 3. Moreover, the distribution is also sorted successively, according to the minimum magnitude used in the recurrence modeling (a and b pair), the interseismic coupling estimate, the rigidity modulus value, and the α value (Fig. 11, following Beauval *et al.*, 2020). The parameters that influence the most the variability on M_{max} are the form of the recurrence model and α—the fraction of the slip deficit that is released seismically.

The limits of this interface source zone correspond, approximately, to the rupture area of the 1906 M_s 8.6 megathrust earthquake (Yepes *et al.*, 2016). Following the analysis of Ye *et al.* (2016), we adopted the Gutenberg and Richter (1954) M_s magnitude 8.6 for the 1906 earthquake and assumed $M_w = M_s$. The magnitude of this megathrust earthquake is

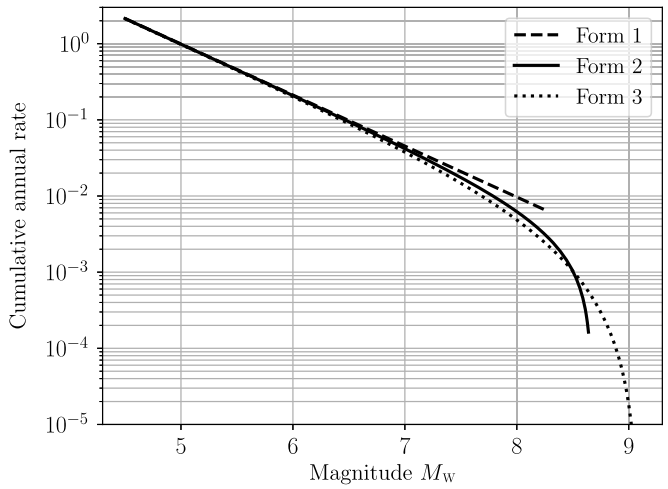

Figure 10. Moment-balanced earthquake recurrence models: strong impact on M_{max} of the form selected. The moment deficit rate is fixed ($\dot{M}_{OG} = 3.92 \times 10^{19}$ N · m/yr), and α is assumed equal to 0.9. The *a*- and *b*-values are kept constant ($a = 3.35$, $b = 0.67$). The three alternative models correspond to the three alternative forms of Anderson and Luco (1983). Forms 1–3 lead to, respectively, M_{max} values of 8.3, 8.7, and 9.1. The color version of this figure is available only in the electronic edition.

the maximum observed magnitude in the known history on this segment and is selected as the minimum bound for M_{max}. All models with M_{max} values lower than 8.6 are not realistic and should be discarded. Form 1 is thus eliminated (Figs. 9 and 11). In addition, to determine an upper bound for M_{max}, we apply the Strasser *et al.* (2010) scaling relationships adapted for interface earthquakes. The equations relying on the length (~580 km), the width (~130 km), and the area lead to magnitude values of, respectively, 9.0, 8.6, and 8.8, considering the mean plus one standard deviation. Therefore, we set the maximum value for an earthquake on the Esmeraldas interface to 9.0. Finally, 89 models out of the 324 obtained have the maximum magnitude within the range 8.6–9.0 (34 associated with Form 2, Fig. 12a, and 55 associated with Form 3, Fig. 12b). The α-values associated with the selected models are also displayed (Fig. 12c,d). As expected, because Form 2 predicts larger seismic rates in the upper-magnitude range than Form 3, α-values associated with Form 2 are larger than α-values associated with Form 3. Considering Form 2, the α-values required for the model to match past seismicity and to be consistent with the moment deficit rate are mostly in the range 0.7–0.9 (i.e., 70%–90% of the interseismic deformation measured will be released in earthquakes), whereas considering Form 3, the barycenter of α-values is around 0.5.

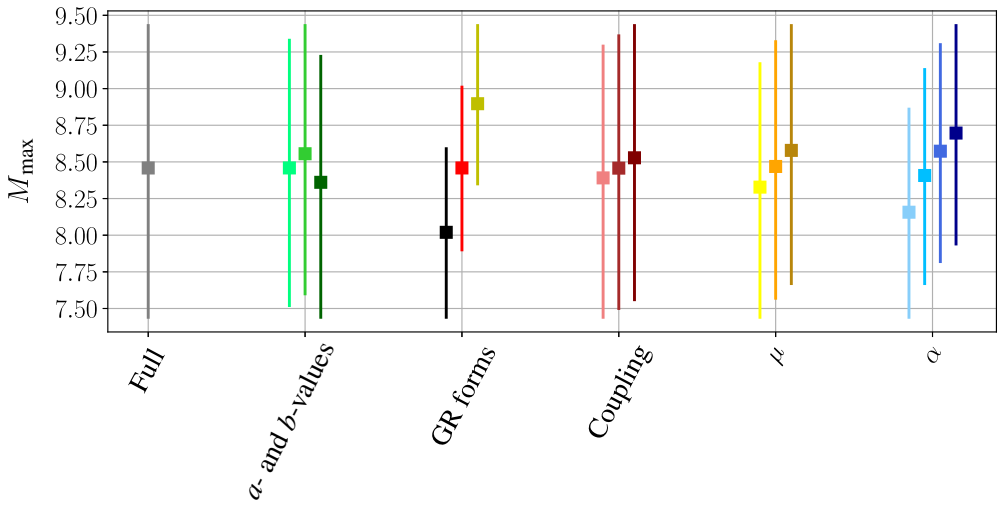

Figure 11. M_{max} values obtained for Esmeraldas interface, exploring uncertainties (see Fig. 8). Mean value (square), the minimum and the maximum values (vertical bar). "Full": complete exploration of uncertainties (324 branches). "*a*- and *b*-values": choice of the minimum magnitude for modeling earthquake recurrence (from left to right): light green M_w 4.5+ (108 branches), green M_w 4.8+ (108 branches), and dark green M_w 5.1+ (108 branches). "GR forms": choice of the form to extrapolate the Gutenberg–Richter model up to M_{max} (from left to right): Form 1 (black, 108 branches), Form 2 (red, 108 branches), and Form 3 (yellow, 108 branches). "Coupling": choice of the interseismic coupling estimates: the minimum (108 branches), the best model (108 branches), the maximum (108 branches), from light pink to dark pink (from left to right). "μ": choice of the shear modulus value (from left to right, 30 GPa in bright yellow, 40 GPa in orange, and 50 GPa in brown, 108 branches each). "α": choice of the α parameter (0.3, 0.5, 0.7, 0.9, from left to right, from light blue to dark blue, 81 branches each). We consider further that the magnitudes lower than 8.6 and larger than 9.0 are unrealistic. The color version of this figure is available only in the electronic edition.

Seismic hazard assessment at Esmeraldas city

We estimate probabilistic seismic hazard at a test site, the Esmeraldas city, in northern Ecuador (latitude: 0.9869° N; longitude: −79.6513° W, Fig. 1). The city hosts oil refineries important for the Ecuadorian economy. It is located at ~24 km from the modeled interface (shortest distance between the city and the slab interface). For this site location on the coast, at 475 yr return period, the seismic sources that control the hazard are subduction interface events (see fig. 8 in Beauval *et al.*, 2018); therefore, we do not include crustal or inslab sources. The set of moment-balanced magnitude–frequency distributions established for the Esmeraldas interface is combined with the Abrahamson *et al.* (2016) ground-motion model, to determine ground-motion exceedance rates. The Abrahamson *et al.* (2016) model has been developed from a global dataset that includes interface earthquakes with magnitudes 6.0–8.4 at distances up

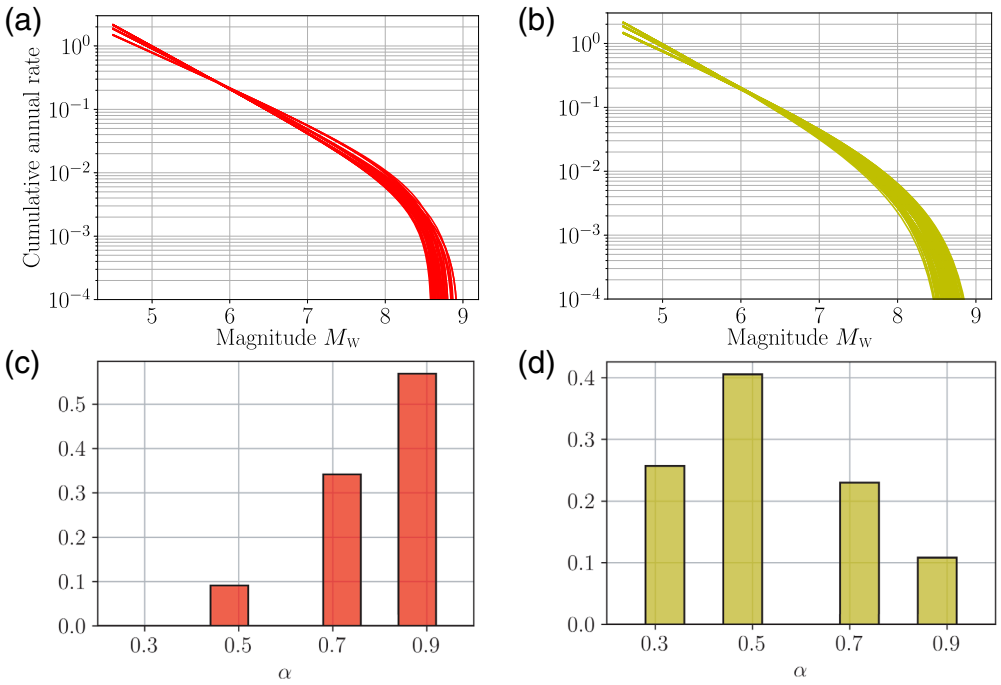

Figure 12. Set of moment-balanced earthquake recurrence models that passes the M_{max} criteria (i.e., with $8.6 \leq M_{max} \leq 9.0$) and associated α-values. (a) 34 models Form 2 pass the M_{max} criteria; (b) 55 models Form 3 pass the M_{max} criteria; (c) distribution of α-values associated with Form 2 models; (d) distribution of α-values associated with Form 3 models. The color version of this figure is available only in the electronic edition.

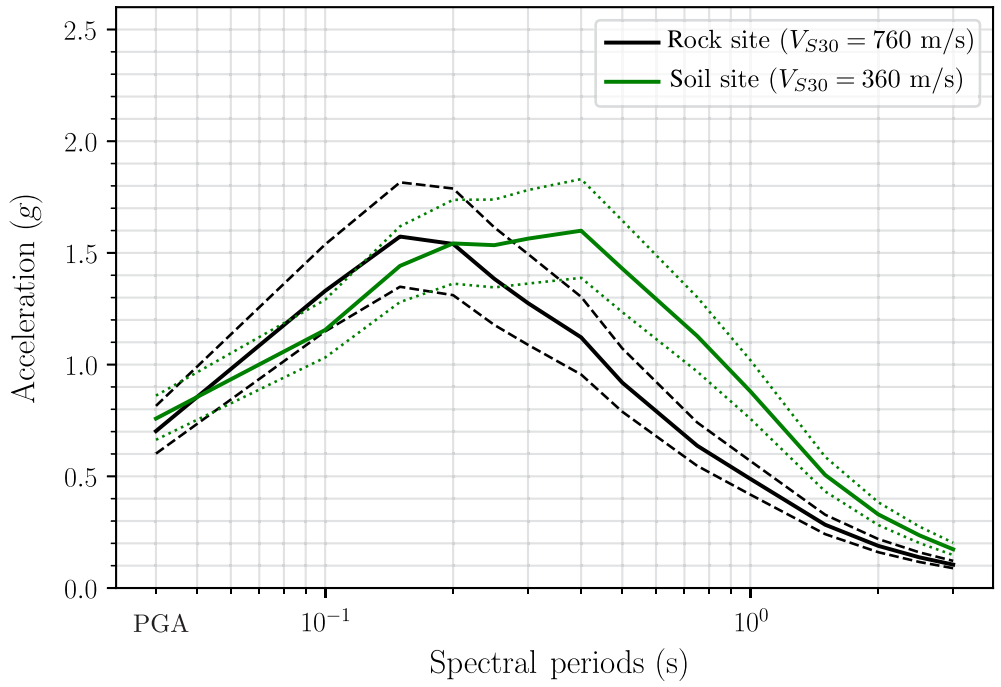

Figure 13. Distribution of uniform hazard spectra (UHS) at 475 yr return period, for a site located in Esmeraldas city. Black: generic rock site (V_{S30} = 760 m/s); green: soil site with V_{S30} = 360 m/s. For each spectral period, the mean (solid line) and 16th and 84th percentiles (dashed lines) are estimated from 89 acceleration values, corresponding to the 89 alternative source models for the Esmeraldas interface fault plane. The ground-motion model used is Abrahamson *et al.* (2016). PGA, peak ground acceleration. The color version of this figure is available only in the electronic edition.

to 300 km. Hazard calculations are performed using the minimum magnitude M_w 4.5, the maximum source-site distance of 300 km, and with the Gaussian distributions predicted by the ground-motion model truncated at $+4\sigma$.

The 89 magnitude–frequency distributions (the A Set of Moment-Balanced Recurrence Models Accounting for Uncertainties section) lead to 89 hazard curves for a given spectral period. Each hazard curve is interpolated to obtain the acceleration corresponding to an annual rate of 1/475. Finally, a series of 89 uniform hazard spectra (UHS) is obtained (Fig. 13); each acceleration has a probability of 10% of being exceeded at least once in a 50 yr time window (equivalent to a mean return period of 475 yr, assuming Poisson occurrences). The hazard is calculated for a generic site on rock (V_{S30} = 760 m/s) and a site on soil (V_{S30} = 360 m/s) (Fig. 13). On rock, mean values of 0.70 and 1.54*g* are obtained at the PGA and spectral period 0.2 s, respectively. The variability of the hazard estimates, resulting from the exploration of uncertainties, is 0.60–0.82*g* and 1.31–1.79*g* at the PGA and 0.2 s, respectively, considering the 16th and 84th percentiles (Fig. 13). Abrahamson *et al.* (2016) model accounts for nonlinear site amplification; the accelerations obtained for a V_{S30} = 360 m/s are lower than the accelerations on rock in the short-period range, and larger in the intermediate- and long-period range.

To understand which magnitudes matter in terms of hazard for a site close to the interface (~24 km for

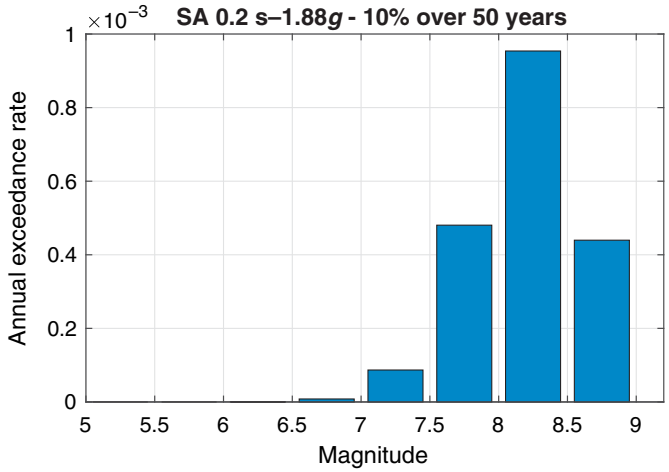

Figure 14. Disaggregation in magnitude using the model Abrahamson *et al.* (2016) to predict the ground motions produced by earthquakes on the interface-dipping segment. Earthquake frequencies are described by a Gutenberg–Richter model with parameters $a = 3.06$, $b = 0.62$, and $M_{max} = 8.7$. The disaggregation is performed for a site in Esmeraldas city, considering the acceleration at 0.2 s spectral period, with a return period of 475 yr (1.88*g*). This disaggregation results show that magnitudes lower than 7.0 have a negligible contribution to the hazard. SA, spectral acceleration. The color version of this figure is available only in the electronic edition.

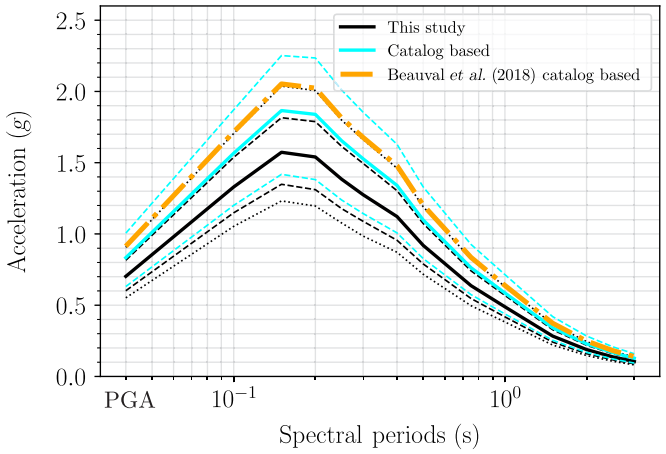

Figure 15. UHS at Esmeraldas city, at 475 yr return period. Black: UHS distribution obtained from this study, solid line: mean values, dashed lines: 16th and 84th percentiles, and dotted lines: 2nd and 98th percentiles. The orange curve represents UHS based on the earthquake recurrence model from Beauval *et al.* (2018) ($a = 2.78$, $b = 0.57$, $M_{max} = 8.8$; global catalog branch). Blue curves represent UHS distribution based on catalog-based recurrence models; the recurrence models are extrapolated up to the maximum magnitude, ignoring the constraints from geodesy. We explore the uncertainties on the *a*- and *b*-values (three couples, Fig. 4c), on the Gutenberg–Richter form (three alternatives) and on the maximum magnitude (five M_{max} values from 8.6 to 9.0), in total 45 end branches. The ground-motion model Abrahamson *et al.* (2016) is used in these calculations. The color version of this figure is available only in the electronic edition.

Esmeraldas city), we perform a disaggregation in magnitude for the two alternative ground-motion models for the spectral period 0.2 s at 475 yr return period (Fig. 14). The results show that most contributions come from earthquakes with magnitudes larger than 7.0–7.5, that is, the part of the recurrence model that bears the largest uncertainties.

COMPARISONS WITH PREVIOUS STUDIES

Comparison with hazard estimates relying on catalog-based recurrence models

In the hazard model derived at the country scale published in Beauval *et al.* (2018), the recurrence models for the interface subduction sources relied only on earthquake catalogs. Gutenberg–Richter recurrence parameters were estimated from past seismicity over the moderate-magnitude range, then extrapolated up to an M_{max} inferred from a scaling relationship applied to the maximum length of the segment, without additional constraints from geodesy. For Esmeraldas, the maximum magnitude of 8.8 was considered. In Figure 15, we superimpose the UHS distribution obtained within the present study to the UHS relying on the recurrence model assumed for Esmeraldas at that time (see fig. 7b in Beauval *et al.*, 2018, recurrence parameters from a global earthquake catalog, Form 2). The UHS based on the 2018 assumptions leads to hazard values that correspond to the 98th percentile of the obtained distribution. Our search for recurrence models matching the seismic moment budget inferred from geodetic measurements leads to lower hazard values (0.6–0.8*g* at the PGA, corresponding to the 16th and 84th percentiles, rather than 0.9*g*).

To better understand these differences in hazard levels, we perform another calculation (Fig. 15). A series of catalog-based recurrence models is generated, in which the recurrence models are extrapolated to the maximum magnitude, ignoring the constraints from geodesy. The models are obtained by exploring the uncertainty on the *a*- and *b*-values (three couples, Fig. 4c), on the Gutenberg–Richter forms (three forms), and on the maximum magnitude (five values, ranging from 8.6 to 9.0). These recurrence models are then combined with the Abrahamson *et al.* (2016) ground-motion model, to evaluate UHS at 475 yr return period. The amplitudes from these catalog-based recurrence models result much higher than the amplitudes relying on moment-balanced recurrence models (Fig. 15, 1.0*g* obtained for the 84th percentile, rather than 0.8*g*, at the PGA).

Comparison with hazard estimates from independent studies

To compare our results with independent studies, we looked for published PSHA studies delivering hazard estimates on the coast. Petersen *et al.* (2018a,b) evaluate seismic hazard at the scale of the South American continent. Because the mean

hazard maps presented are at a large scale, and values displayed in 0.2g bin, we can only infer an approximate acceleration interval of 0.7–0.8g for the PGA at 475 yr for Esmeraldas city (V_{S30} = 760 m/s). This interval falls within our estimation. The subduction interface is modeled as fault segments dipping with 45°; the segmentation considered is less detailed than in the present work. They use two alternative recurrence models for interface events with $M_w \geq 7.5$—a Gutenberg–Richter distribution based on past seismicity with the maximum observed earthquake and a simple characteristic model represented by one megathrust earthquake every 400 yr. (They consider this recurrence time as a first-order approximation for the convergence rate.) Lower-magnitude events are accounted for through a gridded-seismicity model. Because we were interested in the exact hazard curves they obtain at Esmeraldas city, we retrieved all information available online that describes the source model (interface, inslab, and crustal sources) and the ground-motion logic tree (Petersen *et al.*, 2018b, see Data and Resources). We converted this information into OpenQuake format and run the hazard calculation. The results in Esmeraldas city resulted lower (0.5g at the PGA) than what the map tells us. Unfortunately, we could not identify the reason. More work would be required to ensure that our translation into OpenQuake input files is in line with the Petersen *et al.* (2018b) model definition.

In another article focused on subduction sources, Pagani, Johnson, *et al.* (2020) propose a new shape for the magnitude–frequency distribution characterizing earthquake occurrences on interface segments. This distribution is comparable to the Youngs and Coppersmith (1985) characteristic model, with the rates in the upper-magnitude range larger than predicted by the moderate-magnitude range. The upper-magnitude range has a characteristic behavior, the seismic rates being constrained by the convergence rate and the coupling of the interface. They apply this model to the South American subduction zone; however, we cannot compare their seismic rates with our recurrence models, because they use longer interface segments. There are important differences with respect to the present work: (1) they consider the convergence rate of the Nazca plate with respect to South America (58 mm/yr), rather than the motion of the Nazca plate with respect to the NAS (47 mm/yr, Nocquet *et al.*, 2017); (2) they use an average interseismic coupling coefficient of 0.55 and a shear modulus of 32 GPa, taken from Scholz and Campos (2012); and (3) they do not account for transient aseismic deformation. This model has been implemented within the GEM mosaic (Pagani, Garcia-Pelaez, *et al.*, 2020). The UHS obtained combining this source model with the Abrahamson *et al.* (2016) ground-motion model is superimposed to our estimations in Figure 16. Their hazard results are comparable to our 2018 catalog-based estimate (global catalog branch, Beauval *et al.*, 2018).

The interface subduction model from Pagani, Garcia-Pelaez, *et al.* (2020) and Pagani, Johnson, *et al.* (2020) is moment balanced, but it ignores transient aseismic deformation. We perform a last calculation, applying the methodology developed in the A Set of Moment-Balanced Recurrence Models Accounting for Uncertainties section, exploring uncertainties, as detailed in Figure 8, but this time ignoring potential aseismic deformation and assuming $\alpha = 1$. A series of recurrence models is selected, under the condition that the maximum magnitude obtained is within the range 8.6–9.0. As expected, ignoring aseismic deformation leads to higher hazard levels (Fig. 16).

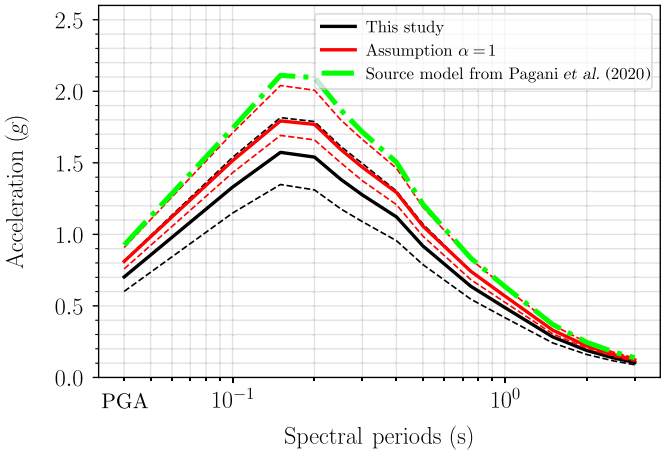

Figure 16. UHS at Esmeraldas city, at 475 yr return period. Black: UHS distribution obtained from this study, solid line: mean values, dashed lines: 16th and 84th percentiles. The green curve represents UHS based on the source model from Pagani, Garcia-Pelaez, *et al.* (2020). Red curves represent comparison with the UHS distribution obtained applying the exact same methodology presented in this article (the A Set of Moment-Balanced Recurrence Models Accounting for Uncertainties section, Fig. 8), but considering $\alpha = 1.0$. Calculations performed with the ground-motion model of Abrahamson *et al.* (2016). The color version of this figure is available only in the electronic edition.

CONCLUSIONS

We propose a method for combining seismic and geodetic data to constrain the recurrence models of earthquakes on the megathrust interface of Ecuador and Colombia. We focus on the Esmeraldas ~600 km long segment, the approximate rupture segment of the 1906 M_w 8.6 earthquake. Available interseismic coupling models for Ecuador (Chlieh *et al.*, 2014; Nocquet *et al.*, 2014) have been extended to Colombia up to latitude 4° N, to determine the moment deficit rate that accumulates on the slab interface. We select the coastal city Esmeraldas, as an example site located above the dipping segment in which probabilistic seismic hazard is estimated.

In the Esmeraldas source zone, the observed instrumental rates show an exponential decrease with increasing magnitude over the magnitude range 4.5–7. Our strategy relies on anchoring a Gutenberg–Richter model to these moderate magnitude rates and extrapolate the model up to the maximum magnitude. We look for moment-balanced recurrence models, that is,

models that fit the seismic moment estimated from geodesy, by adjusting the maximum magnitude bounding the Gutenberg–Richter model (M_{max}).

A set of moment-balanced recurrence models with associated M_{max} is obtained, by exploring uncertainties characterizing the recurrence model (a- and b-values, extrapolation to M_{max}) as well as uncertainties underlying the estimation of the tectonic deformation to be released in earthquakes (coupling model; shear modulus, seismic vs. aseismic slip). We show that the uncertainties influencing the most the recurrence model are:

- the fraction of the slip deficit that will be released in earthquakes (α-value) and
- the form of the Gutenberg–Richter model close to M_{max}.

We keep only the models associated with a realistic M_{max}, that is, within the largest observed event in the zone and an upper bound inferred from a scaling law. Finally, we obtain a distribution of UHS at Esmeraldas city, by combining this subset of recurrence models with the Abrahamson *et al.* (2016) ground-motion model. We show that the moment-balanced models obtained lead on average to lower hazard values than the earthquake recurrence models relying only on seismicity data.

The use of geodetic data to constrain a long-term earthquake recurrence mode for PSHA implies strong assumptions, in particular, that the deformation measured over a short-time windows, is steady and representative of long-term processes. However, given the uncertainty to forecast rates in the upper-magnitude range ($M_w \geq 7.0$), the geodetic deformation measurements provide key constraints on this part of the recurrence model that controls the hazard at coastal sites.

Considering the recent availability of massive quantity of geodetic data, this new approach could be applied in other regions of the world to develop earthquake recurrence models consistent with geodetic measurements of tectonic deformation.

DATA AND RESOURCES

The Global Centroid Moment Tensor (Global CMT) database was available at ~https://www.ldeo.columbia.edu/~gcmt/projects/CMT/catalog/jan76_dec17.ndk. The International Seismological Centre–Global Earthquake Model (ISC-GEM) Global Instrumental Earthquake Catalog (1904–2016) version 7.0 (v.7.0) was available at http://www.isc.ac.uk/iscgem/download.php. The bulletin of the ISC was available at http://www.isc.ac.uk/iscbulletin/search/bulletin/ (corresponding to a reviewed period until September 2017). The source model and the ground-motion logic tree from Petersen *et al.* (2018b) are accessible at https://www.sciencebase.gov/catalog/item/58795a8ce4b04df303d97ed8. The source model from Pagani, Garcia-Pelaez, *et al.* (2020) is accessible at https://hazard.openquake.org/gem/. All websites were last accessed in April 2020.

DECLARATION OF COMPETING INTERESTS

The authors acknowledge that there are no conflicts of interest recorded.

ACKNOWLEDGMENTS

This research was supported by the French Agence Nationale de la Recherche (ANR) through the project REMAKE (2016–2019, Grant Number ANR-15-CE04-004), by the Institut de Recherche pour le Développement (IRD), the Geophysical Institute in Quito part of the Escuela Politecnica Nacional, as well as ISTerre and Géoazur Laboratories. We thank the project SEMPLADES (Generación de capacidades para la difusión de alertas tempranas y para el desarrollo de instrumentos de decisión ante las amenazas sísmicas y volcánicas dirigidos al Sistema Nacional de Gestión de Riesgos). This work has been carried out in the frame of the Joint International Laboratory "Seismes & Volcans dans les Andes du Nord" (IRD LMI SVAN). We are grateful to Editor Mark Stirling as well as to Marco Pagani and an anonymous reviewer for their careful review. We are also grateful to the Global Earthquake Model Foundation and to the IT ISTerre team for constant support on the OpenQuake Engine software and server.

REFERENCES

Abe, K. (1981). Magnitudes of large shallow earthquakes from 1904 to 1980, *Phys. Earth Planet. In.* **27,** no. 1, 72–92.

Abrahamson, N., N. Gregor, and K. Addo (2016). BC hydro ground motion prediction equations for subduction earthquakes, *Earthq. Spectra* **32,** no. 1, 23–44.

Alvarado, A., L. Audin, J.-M. Nocquet, E. Jaillard, P. Mothes, P. Jarrín, M. Segovia, F. Rolandone, and D. Cisneros (2016). Partitioning of oblique convergence in the northern Andes subduction zone: Migration history and the present-day boundary of the North Andean Sliver in Ecuador: Eastern limit of the North Andean Sliver, *Tectonics* **35,** no. 5, 1048–1065.

Anderson, J. G. (1979). Estimating the seismicity from geological structure for seismic-risk studies, *Bull. Seismol. Soc. Am.* **69,** no. 1, 135–158.

Anderson, J. G., and J. E. Luco (1983). Consequences of slip rate constraints on earthquake occurrence relations, *Bull. Seismol. Soc. Am.* **73,** no. 2, 471–496.

Avouac, J.-P. (2015). From geodetic imaging of seismic and aseismic fault slip to dynamic modeling of the seismic cycle, *Annu. Rev. Earth Planet. Sci.* **43,** no. 1, 233–271.

Beauval, C., P.-Y. Bard, and L. Danciu (2020). The influence of source- and ground-motion model choices on probabilistic seismic hazard levels at 6 sites in France, *Bull. Earthq. Eng.* **18,** no. 10, 4551–4580.

Beauval, C., J. Marinière, A. Laurendeau, J.-C. Singaucho, C. Viracucha, M. Vallée, E. Maufroy, D. Mercerat, H. Yepes, M. Ruiz, *et al.* (2017). Comparison of observed ground-motion attenuation for the 16 April 2016 M_w 7.8 Ecuador megathrust earthquake and its two largest aftershocks with existing ground-motion prediction equations, *Seismol. Res. Lett.* **88,** no. 2A, 287–299.

Beauval, C., J. Marinière, H. Yepes, L. Audin, J.-M. Nocquet, A. Alvarado, S. Baize, J. Aguilar, J.-C. Singaucho, and H. Jomard (2018). A new seismic hazard model for Ecuador, *Bull. Seismol. Soc. Am.* **108,** no. 3A, 1443–1464.

Beauval, C., and O. Scotti (2003). Mapping b-values in France using two different magnitude ranges: Possible non power-law behavior, *Geophys. Res. Lett.* **30,** no. 17, doi: 10.1029/2003GL017576.

Beauval, C., H. Yepes, L. Audin, A. Alvarado, J.-M. Nocquet, D. Monelli, and L. Danciu (2014). Probabilistic seismic-hazard assessment in Quito, estimates and uncertainties, *Seismol. Res. Lett.* **85,** no. 6, 1316–1327.

Beauval, C., H. Yepes, P. Palacios, M. Segovia, A. Alvarado, Y. Font, J. Aguilar, L. Troncoso, and S. Vaca (2013). An earthquake catalog for seismic hazard assessment in Ecuador, *Bull. Seismol. Soc. Am.* **103,** no. 2A, 773–786.

Bilek, S. L., and T. Lay (1999). Rigidity variations with depth along interplate megathrust faults in subduction zones, *Nature* **400,** no. 6743, 443–446.

Brax, M., P. Albini, C. Beauval, R. Jomaa, and A. Sursock (2019). An earthquake catalog for the Lebanese region, *Seismol. Res. Lett.* **90,** no. 6, 2236–2249.

Brune, J. N. (1968). Seismic moment, seismicity, and rate of slip along major fault zones, *J. Geophys. Res.* **73,** no. 2, 777–784.

Chlieh, M., P. A. Mothes, J.-M. Nocquet, P. Jarrin, P. Charvis, D. Cisneros, Y. Font, J.-Y. Collot, J.-C. Villegas-Lanza, F. Rolandone, *et al.* (2014). Distribution of discrete seismic asperities and aseismic slip along the Ecuadorian megathrust, *Earth Planet. Sci. Lett.* **400,** 292–301.

Chlieh, M., H. Perfettini, H. Tavera, J.-P. Avouac, D. Remy, J.-M. Nocquet, F. Rolandone, F. Bondoux, G. Gabalda, and S. Bonvalot (2011). Interseismic coupling and seismic potential along the central Andes subduction zone, *J. Geophys. Res.* **116,** no. B12, doi: 10.1029/2010JB008166.

D'Agostino, N. (2014). Complete seismic release of tectonic strain and earthquake recurrence in the Apennines (Italy), *Geophys. Res. Lett.* **41,** no. 4, 1155–1162.

Di Giacomo, D., I. Bondár, D. A. Storchak, E. R. Engdahl, P. Bormann, and J. Harris (2015). ISC-GEM: Global Instrumental Earthquake Catalogue (1900–2009), III. Re-computed M_s and m_b, proxy M_w, final magnitude composition and completeness assessment, *Phys. Earth Planet. In.* **239,** 33–47.

Dziewonski, A. M., T.-A. Chou, and J. H. Woodhouse (1981). Determination of earthquake source parameters from waveform data for studies of global and regional seismicity, *J. Geophys. Res.* **86,** no. B4, 2825–2852.

Egred, J. (2009). Catalogo de Terremotos del Ecuador 1541–2009, *Internal Report*, Instituto Geofisico, Escuela Politecnica Nacional, Quito (in Spanish).

Ekström, G., M. Nettles, and A. M. Dziewoński (2012). The Global CMT project 2004–2010: Centroid-moment tensors for 13,017 earthquakes, *Phys. Earth Planet. In.* **200/201,** 1–9.

Field, E. H., D. D. Jackson, and J. F. Dolan (1999). A mutually consistent seismic-hazard source model for southern California, *Bull. Seismol. Soc. Am.* **89,** no. 3, 559–578.

Font, Y., M. Segovia, S. Vaca, and T. Theunissen (2013). Seismicity patterns along the Ecuadorian subduction zone: New constraints from earthquake location in a 3-D a priori velocity model, *Geophys. J. Int.* **193,** no. 1, 263–286.

Gailler, A., P. Charvis, and E. R. Flueh (2007). Segmentation of the Nazca and South American plates along the Ecuador subduction zone from wide angle seismic profiles, *Earth Planet. Sci. Lett.* **260,** nos. 3/4, 444–464.

Gardner, J. K., and L. Knopoff (1974). Is the sequence of earthquakes in southern California, with aftershocks removed, Poissonian?, *Bull. Seismol. Soc. Am.* **64,** no. 5, 1363–1367.

Gombert, B., Z. Duputel, R. Jolivet, M. Simons, J. Jiang, C. Liang, E. J. Fielding, and L. Rivera (2018). Strain budget of the Ecuador–Colombia subduction zone: A stochastic view, *Earth Planet. Sci. Lett.* **498,** 288–299.

Graindorge, D. (2004). Deep structures of the Ecuador convergent margin and the Carnegie ridge, possible consequence on great earthquakes recurrence interval, *Geophys. Res. Lett.* **31,** no. 4, doi: 10.1029/2003GL018803.

Grünthal, G., D. Stromeyer, C. Bosse, F. Cotton, and D. Bindi (2018). The probabilistic seismic hazard assessment of Germany—Version 2016, considering the range of epistemic uncertainties and aleatory variability, *Bull. Earthq. Eng.* **16,** no. 10, 4339–4395.

Gutenberg, B., and C. F. Richter (1944). Frequency of earthquakes in California, *Bull. Seismol. Soc. Am.* **34,** no. 4, 185–188.

Gutenberg, B., and C. F. Richter (1954). *Seismicity of the Earth and Associated Phenomena*, Princeton University Press, Princeton, New Jersey, 310 pp.

Hanks, T. C., and H. Kanamori (1979). A moment magnitude scale, *J. Geophys. Res.* **84,** no. B5, 2348.

Hayes, G. P., D. J. Wald, and R. L. Johnson (2012). Slab1.0: A three-dimensional model of global subduction zone geometries, *J. Geophys. Res.* **117,** no. B1, doi: 10.1029/2011JB008524.

Hyndman, R. D., S. Mazzotti, D. Weichert, and G. C. Rogers (2003). Frequency of large crustal earthquakes in Puget Sound–southern Georgia Strait predicted from geodetic and geological deformation rates: GPS and earthquakes in the Pacific Northwest, *J. Geophys. Res.* **108,** no. B1, doi: 10.1029/2001JB001710.

International Seismological Centre (ISC) (2020). On-line bulletin. http://www.isc.ac.uk/iscbulletin/search/bulletin/ (last accessed April 2020).

Kagan, Y. Y. (2002). Seismic moment distribution revisited: I. Statistical results, *Geophys. J. Int.* **148,** no. 3, 520–541.

Kagan, Y. Y., and D. D. Jackson (2013). Tohoku earthquake: A surprise? *Bull. Seismol. Soc. Am.* **103,** no. 2B, 1181–1194.

Keller, E. (2014). Caractérisation de Séismes Historiques. Application sur les Grands Séismes de Subduction en Équateur, Mémoire de stage de Master 2, Master SML, UBO (in French).

Lolli, B., P. Gasperini, and G. Vannucci (2014). Empirical conversion between teleseismic magnitudes (m_b and M_s) and moment magnitude (M_w) at the Global, Euro-Mediterranean and Italian scale, *Geophys. J. Int.* **199,** no. 2, 805–828.

Marzocchi, W., L. Sandri, A. Heuret, and F. Funiciello (2016). Where giant earthquakes may come, *J. Geophys. Res.* **121,** no. 10, 7322–7336.

Mazzotti, S., L. J. Leonard, J. F. Cassidy, G. C. Rogers, and S. Halchuk (2011). Seismic hazard in western Canada from GPS strain rates versus earthquake catalog, *J. Geophys. Res.* **116,** no. B12, doi: 10.1029/2011JB008213.

Medina, F., S. C. Harmsen, and S. E. Barrientos (2017). Probabilitic seismic hazard analysis for Chile, *16th World Conf. on Earthquake Engineering*, Santiago, Chile, 9–13 January.

Michel, S., J. Avouac, R. Jolivet, and L. Wang (2018). Seismic and aseismic moment budget and implication for the seismic potential of the Parkfield segment of the San Andreas fault, *Bull. Seismol. Soc. Am.* **108,** no. 1, 19–38.

Migeon, S., C. Garibaldi, G. Ratzov, S. Schmidt, J.-Y. Collot, S. Zaragosi, and L. Texier (2017). Earthquake-triggered deposits in the subduction trench of the north Ecuador/south Colombia margin and their implication for paleoseismology, *Mar. Geol.* **384,** 47–62.

Mihaljević, J., P. Zupančič, N. Kuka, N. Kaluđerović, R. Koçi, S. Markušić, R. Šalić, E. Dushi, E. Begu, L. Duni, *et al.* (2017). BSHAP seismic source characterization models for the western Balkan region, *Bull. Earthq. Eng.* **15,** no. 10, 3963–3985.

Molnar, P. (1979). Earthquake recurrence intervals and plate tectonics, *Bull. Seismol. Soc. Am.* **69,** no. 1, 115–133.

Mothes, P. A., J.-M. Nocquet, and P. Jarrín (2013). Continuous GPS network operating throughout Ecuador, *Eos Trans. AGU* **94,** no. 26, 229–231.

Nocquet, J.-M. (2018). Stochastic static fault slip inversion from geodetic data with non-negativity and bounds constraints, *Geophys. J. Int.* **214,** no. 1, 366–385.

Nocquet, J.-M., P. Jarrin, M. Vallée, P. A. Mothes, R. Grandin, F. Rolandone, B. Delouis, H. Yepes, Y. Font, D. Fuentes, *et al.* (2017). Supercycle at the Ecuadorian subduction zone revealed after the 2016 Pedernales earthquake, *Nature Geosci.* **10,** no. 2, 145–149.

Nocquet, J.-M., J. C. Villegas-Lanza, M. Chlieh, P. A. Mothes, F. Rolandone, P. Jarrin, D. Cisneros, A. Alvarado, L. Audin, F. Bondoux, *et al.* (2014). Motion of continental slivers and creeping subduction in the northern Andes, *Nature Geosci.* **7,** no. 4, 287–291.

Pagani, M., J. Garcia-Pelaez, R. Gee, K. Johnson, V. Poggi, V. Silva, M. Simionato, R. Styron, D. Viganó, L. Danciu, *et al.* (2020). The 2018 version of the Global Earthquake Model: Hazard component, *Earthq. Spectra* doi: 10.1177/8755293020931866.

Pagani, M., K. Johnson, and J. Garcia-Pelaez (2020). Modelling subduction sources for probabilistic seismic hazard analysis, *Geol. Soc. Lond. Spec. Publ.* doi: 10.1144/SP501-2019-120.

Pagani, M., D. Monelli, G. Weatherill, L. Danciu, H. Crowley, V. Silva, P. Henshaw, L. Butler, M. Nastasi, L. Panzeri, *et al.* (2014). OpenQuake engine: An open hazard (and risk) software for the Global Earthquake Model, *Seismol. Res. Lett.* **85,** no. 3, 692–702.

Pancha, A., J. G. Anderson, and C. Kreemer (2006). Comparison of seismic and geodetic scalar moment rates across the Basin and Range Province, *Bull. Seismol. Soc. Am.* **96,** no. 1, 11–32.

Pacific Earthquake Engineering Research Center (PEER) Report (2020). Data resources for NGA-Subduction Project, Bozorgnia, Yousef (NGA-Subduction Principal Investigator) and Jonathan P. Stewart (Report Editor), *PEER Report 2020/02*, Pacific Earthquake Engineering Research Center, University of California, Berkeley, California.

Pennington, W. D. (1981). Subduction of the eastern Panama basin and seismotectonics of northwestern South America, *J. Geophys. Res.* **86,** no. B11, 10,753–10,770.

Petersen, M. D., A. D. Frankel, S. C. Harmsen, C. S. Mueller, K. M. Haller, R. L. Wheeler, E. L. Wesson, Y. Zeng, O. S. Boyd, D. M. Perkins, *et al.* (2008). Documentation for the 2008 update of the United States National Seismic Hazard Maps, *Report 2008-1128*, version 1.0: April 2008; version 1.1: May 2008, Reston, Virginia, doi: 10.3133/ofr20081128.

Petersen, M. D., S. C. Harmsen, K. S. Jaiswal, K. S. Rukstales, N. Luco, K. M. Haller, C. S. Mueller, and A. M. Shumway (2018a). Seismic hazard, risk, and design for South America, *Bull. Seismol. Soc. Am.* **108,** no. 2, 781–800.

Petersen, M. D., S. C. Harmsen, K. S. Jaiswal, K. S. Rukstales, N. Luco, K. M. Haller, C. S. Mueller, and A. M. Shumway (2018b). Seismic hazard, risk, and design for South America, *U.S. Geol. Surv. Data Release.*

Proust, J. N., C. Martillo, F. Michaud, J. Y. Collot, and O. Dauteuil (2016). Subduction of seafloor asperities revealed by a detailed stratigraphic analysis of the active margin shelf sediments of central Ecuador, *Mar. Geol.* **380,** 345–362.

Reasenberg, P. (1985). Second-order moment of central California seismicity, 1969–1982, *J. Geophys. Res.* **90,** no. B7, 5479–5495.

Rolandone, F., J.-M. Nocquet, P. A. Mothes, P. Jarrin, M. Vallée, N. Cubas, S. Hernandez, M. Plain, S. Vaca, and Y. Font (2018). Areas prone to slow slip events impede earthquake rupture propagation and promote afterslip, *Sci. Adv.* **4,** no. 1, eaao6596.

Rong, Y., D. D. Jackson, H. Magistrale, and C. Goldfinger (2014). Magnitude limits of subduction zone earthquakes, *Bull. Seismol. Soc. Am.* **104,** no. 5, 2359–2377.

Sagaiya, T., and H. Mora-Páez (2020). Interplate coupling along the Nazca subduction zone on the Pacific coast of Colombia deduced from GeoRED GPS observation data, in *The Geology of Colombia*, J. Gómez and A. O. Pinilla–Pachon (Editors), Vol. 4 Quaternary, Servicio Geológico Colombiano, Publicaciones Geológicas Especiales 38, Bogotá, Colombia, 15 pp., doi: 10.32685/pub.esp.38.2019.15.

Savage, J. C. (1983). A dislocation model of strain accumulation and release at a subduction zone, *J. Geophys. Res.* **88,** no. B6, 4984–4996.

Scala, A., S. Lorito, F. Romano, S. Murphy, J. Selva, R. Basili, A. Babeyko, A. Herrero, A. Hoechner, F. Løvholt, *et al.* (2020). Effect of shallow slip amplification uncertainty on probabilistic tsunami hazard analysis in subduction zones: Use of long-term balanced stochastic slip models, *Pure Appl. Geophys.* **177,** no. 3, 1497–1520.

Scholz, C. H., and J. Campos (2012). The seismic coupling of subduction zones revisited, *J. Geophys. Res.* **117,** no. B5, doi: 10.1029/2011JB009003.

Secretaria de Gestion de Riesgos (SGR) (2016). Informe de Situacion N°65—16/05/2016 Terremoto 7.8°—Pedernales (in Spanish), available at https://www.google.com/url?sa=t&rct=j&q=&esrc=s&source=web&cd=&ved=2ahUKEwj7t_WA98HvAhUhA2MBHX2cC_gQFjAAegQIAhAD&url=https%3A%2F%2Fwww.gestionderiesgos.gob.ec%2Fwp-content%2Fuploads%2Fdownloads%2F2016%2F05%2FInforme-de-situaci%25C3%25B3n-n%25C2%25B065-especial-16-05-20161.pdf&usg=AOvVaw0jShnhhI0wH6ox2Aqydzu8 (last access April 2020).

Staller, A., J. Álvarez-Gómez, M. Luna, M. Bejar, J. Gaspar-Escribano, and S. Martínez-Cuevas (2018). Crustal motion and deformation in Ecuador from cGNSS time series, *J. S. Am. Earth Sci.* **86,** 94–109.

Stevens, V. L., and J.-P. Avouac (2016). Millenary M_w>9.0 earthquakes required by geodetic strain in the Himalaya, *Geophys. Res. Lett.* **43,** no. 3, 1118–1123.

Stevens, V. L., and J.-P. Avouac (2017). Determination of M_{max} from background seismicity and moment conservation, *Bull. Seismol. Soc. Am.* **107,** no. 6, 2578–2596.

Stevens, V. L., S. N. Shrestha, and D. K. Maharjan (2018). Probabilistic seismic hazard assessment of Nepal, *Bull. Seismol. Soc. Am.* **108,** no. 6, 3488–3510.

Stirling, M., G. McVerry, M. Gerstenberger, N. Litchfield, R. Van Dissen, K. Berryman, P. Barnes, L. Wallace, P. Villamor, R. Langridge, *et al.* (2012). National Seismic Hazard Model for New Zealand: 2010 update, *Bull. Seismol. Soc. Am.* **102,** no. 4, 1514–1542.

Storchak, D. A., D. Di Giacomo, E. R. Engdahl, J. Harris, I. Bondár, W. H. K. Lee, P. Bormann, and A. Villaseñor (2015). The ISC-GEM Global Instrumental Earthquake Catalogue (1900–2009): Introduction, *Phys. Earth Planet. In.* **239,** 48–63.

Storchak, D. A., J. Harris, L. Brown, K. Lieser, B. Shumba, R. Verney, D. Di Giacomo, and E. I. M. Korger (2017). Rebuild of the bulletin of the International Seismological Centre (ISC), part 1: 1964–1979, *Geosci. Lett.* **4,** no. 1, 32.

Strasser, F. O., M. C. Arango, and J. J. Bommer (2010). Scaling of the source dimensions of interface and intraslab subduction-zone earthquakes with moment magnitude, *Seismol. Res. Lett.* **81,** no. 6, 941–950.

Tarantola, A. (2005). *Inverse Problem Theory and Methods for Model Parameter Estimation*, Society for Industrial and Applied Mathematics, doi: 10.1137/1.9780898717921.

Teng, G., and J. W. Baker (2019). Seismicity declustering and hazard analysis of the Oklahoma–Kansas region, *Bull. Seismol. Soc. Am.* **109,** no. 6, 2356–2366.

Vaca, S., M. Vallée, J.-M. Nocquet, and A. Alvarado (2019). Active deformation in Ecuador enlightened by a new waveform-based catalog of earthquake focal mechanisms, *J. S. Am. Earth Sci.* **93,** 449–461.

Vaca, S., M. Vallée, J.-M. Nocquet, J. Battaglia, and M. Régnier (2018). Recurrent slow slip events as a barrier to the northward rupture propagation of the 2016 Pedernales earthquake (central Ecuador), *Tectonophysics* **724/725,** 80–92.

Ward, S. N. (1994). A multidisciplinary approach to seismic hazard in southern California, *Bull. Seismol. Soc. Am.* **84,** no. 5, 1293–1309.

Weichert, D. H. (1980). Estimation of the earthquake recurrence parameters for unequal observation periods for different magnitudes, *Bull. Seismol. Soc. Am.* **70,** no. 4, 1337–1346.

Ye, L., H. Kanamori, J.-P. Avouac, L. Li, K. F. Cheung, and T. Lay (2016). The 16 April 2016, M7.8 (M7.5) Ecuador earthquake: A quasi-repeat of the 1942 M7.5 earthquake and partial re-rupture of the 1906 M8.6 Colombia–Ecuador earthquake, *Earth Planet. Sci. Lett.* **454,** 248–258.

Yepes, H., L. Audin, A. Alvarado, C. Beauval, J. Aguilar, Y. Font, and F. Cotton (2016). A new view for the geodynamics of Ecuador: Implication in seismogenic source definition and seismic hazard assessment: Ecuador geodynamics and PSHA, *Tectonics* **35,** no. 5, 1249–1279.

Youngs, R. R., and K. J. Coppersmith (1985). Implications of fault slip rates and earthquake recurrence models to probabilistic seismic hazard estimates, *Int. J. Rock Mech. Min. Sci. Geomech. Abstr.* **23,** no. 4, 125.

Zöller, G. (2013). Convergence of the frequency-magnitude distribution of global earthquakes: Maybe in 200 years: Frequency–magnitude distribution, *Geophys. Res. Lett.* **40,** no. 15, 3873–3877.

APPENDIX

An earthquake catalog for seismic hazard assessment in Ecuador

We develop an earthquake catalog for seismic hazard assessment in Ecuador, using global catalogs, following the approach described in Beauval *et al.* (2018). The spatial window extends from −82° to −74° in longitudes and from −7° to 4° in latitudes. The catalog extends from 1906 to September 2017.

We select solutions from several published catalogs: the International Seismological Centre–Global Earthquake Model (ISC-GEM) (1904–2016) version 7.0 (v.7.0), the Global Centroid Moment Tensor (Global CMT) catalog (1976–2017, Dziewonski *et al.*, 1981; Ekström *et al.*, 2012), and the ISC event

TABLE A1
Content of the Final Earthquake Catalog Homogenized in Moment Magnitude

Catalog	Author	Type of Magnitude	Minimum Magnitude	Maximum Magnitude	Minimum Year	Maximum Year	Total Number of Events
ISC-GEM	Various	M_w	5.1	8.75*	1906	2016	268
ISC-GEM	Global CMT	M_w	5.0	8.1	1965	2016	191
ISC-GEM supplement†	Various	M_w	5.6	6.5	1917	1966	5
Global CMT	Global CMT	M_w	4.8	6.0	1980	2017	100
ISC-REV	Global CMT	M_w	4.7	5.6	1977	2017	62
ISC-REV	ISC	Proxy M_w from m_b	3.7	6.0	1964	2017	2757
ISC-REV	NEIC	Proxy M_w from m_b	3.7	5.6	1985	2017	217
ISC-REV	NEIS	Proxy M_w from m_b	3.8	6.2	1971	1984	153
ISC-REV	USCGS	Proxy M_w from m_b	3.8	4.8	1964	1970	32
ISC-REV	ABE1	m_b surrogate for M_w	6.9	7.5	1906	1937	3
ISC-REV	PAS	M_s surrogate for M_w	6.8	6.8	1925	1950	3
ISC-REV	PAS	M surrogate for M_w	6.5	6.6	1954	1958	3
Vaca *et al.* (2019)‡	Vaca *et al.* (2019)	M_w	3.6	5.1	2009	2015	74

Magnitude m_b is converted in M_w, applying $M_w = e^{0.741+0.210m_b} - 0.785$ (Lolli *et al.*, 2014, global equation).
ABE1, Abe (1981); Global CMT, Global Centroid Moment Tensor; ISC-GEM, International Seismological Centre–Global Earthquake Model; ISC-REV, the manually reviewed bulletin from the ISC; NEIC - NEIS, National Earthquake Information Center - National Earthquake Information Service; PAS, Gutenberg and Richter (1954); USCGS, U.S. Coast and Geodetic Survey.
*8.75 is the magnitude of the 31 January 1906 megathrust earthquake; we substitute this magnitude with 8.6 in our final catalog (M_s magnitude proxy for M_w, Gutenberg and Richter, 1954; Ye *et al.*, 2016).
†ISC-GEM supplement: The supplementary catalog contains those earthquakes that are believed to be large enough, yet either their location or magnitude or both are highly uncertain due to lack or contradiction in available arrival time or amplitude and period data (Di Giacomo *et al.*, 2015).
‡Vaca *et al.* (2019) is the only regional catalog considered; earthquakes are located from −6° to 2° in latitude and from −83° to −76° in longitude.

reviewed catalog (1906–2017, Storchak *et al.*, 2017; ISC, 2020). In addition, we have included the solutions from Vaca *et al.* (2019), moment magnitudes estimated for earthquakes between 2009 and 2015, in the spatial window from −6° to 2° in latitude and from −83° to −76° in longitude.

The "best" location and the "best" magnitude must be selected for each earthquake, among available solutions. The priority scheme is the following for selecting the magnitude: ISC-GEM M_w > Global CMT M_w > Vaca *et al.* (2019) M_w > ISCm_b > National Earthquake Information Center (NEIC) m_b (or National Earthquake Information Service [NEIS] m_b, or U.S. Coast and Geodetic Survey [USCGS] m_b). Magnitudes ISC-GEM are always associated with the locations from the same catalog. Magnitudes from Vaca *et al.* (2019) are also associated with the locations from the same author. The ISC locations are used for the other events. In the early instrumental period (before 1964), there are nine events appearing in the ISC event catalog that are not included in the ISC-GEM. We keep them and make use of M_s newly determined by the ISC, as well as m_b magnitudes by ABE1 (Abe, 1981) and magnitudes estimated by Gutenberg and Richter (1954, "PAS").

We use the Lolli *et al.* (2014) global equation to convert m_b magnitudes into proxy M_w. Lolli *et al.* (2014) equation is preferred over the Di Giacomo *et al.* (2015) conversion equation (only valid for $M_w > 5.0$). The final catalog includes 3868 events above M_w 3.6 (Table A1). The bulk of the data are made of ISC m_b magnitudes (71%).

Finally, we apply the Reasenberg (1985) algorithm to identify clustered events (foreshocks, aftershocks, and swarms). About 23% of events are removed. The final declustered catalog includes 2978 earthquakes with $M_w \geq 3.6$.

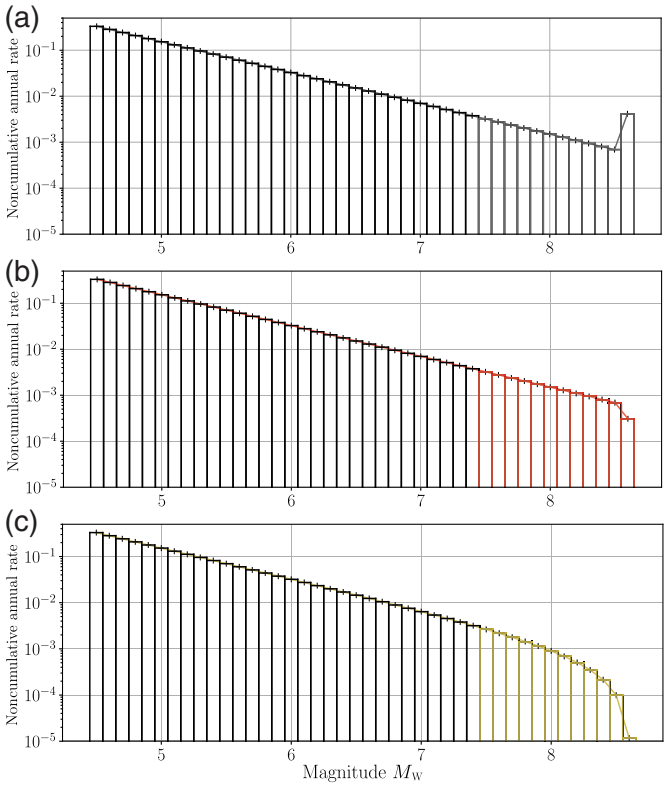

Figure A1. (a–c) Discrete noncumulative seismic rates considering Forms 1–3 in Anderson and Luco (1983). The recurrence parameters correspond to the Esmeraldas source zone ($a = 3.35$, $b = 0.67$). The color version of this figure is available only in the electronic edition.

M_{max} ensuring a moment-balanced earthquake recurrence model

We assume that the magnitude–frequency distribution follows the Anderson and Luco (1983) Form 2. N is the annual rate of events, with magnitude larger or equal to m:

$$N(m) = 10^{a-bm} - 10^{a-bM\,\max} \qquad \text{for } m \leq M_{\max}. \tag{A1}$$

Its derivative provides the annual rate of events with magnitude equal to m:

$$n(m) = b\ln(10)10^{a-bm}. \tag{A2}$$

Hanks and Kanamori (1979) derived the relation:

$$\log_{10}(M_0) = 1.5M_w + 16.1 \quad (\text{dyn}\cdot\text{cm}). \tag{A3}$$

Equation (A3) results in the following relation in N · m (1 dyn · cm = 10^{-7} N · m):

$$M_0(m) = 10^{cm+d}, \tag{A4}$$

in which $c = 1.5$ and $d = 9.1$ for M_0 in units of N · m.

The total seismic moment rate corresponding to the magnitude–frequency distribution is:

$$\dot{M}_0^T = \int_{-\infty}^{M_{\max}} M_0(m)n(m)dm. \tag{A5}$$

Integrating from −∞ up to M_{max} or from M_w 4.5 up to M_{max} is equivalent, because the magnitudes lower than 4.5 have a negligible contribution to the total seismic moment rate ($M_{max} \geq 8.6$).

$$\dot{M}_0^T = 10^{a+d}b\ln(10)\int_{-\infty}^{M_{\max}} 10^{(c-b)m}dm, \tag{A6}$$

$$\dot{M}_0^T = \frac{b}{c-b}10^{a+d+(c-b)M_{\max}}. \tag{A7}$$

Therefore, if there is an independent estimate for the seismic moment rate, for example, from geodesy, $\dot{M}_{0G}$,

TABLE A2
Input Parameters for the Reasenberg (1985) Algorithm

τ_{min} (in days)	10	Uncertainty on event location–after 1970–horizontal	5 km
τ_{max} (in days)	30	Uncertainty on event location—after 1970—vertical	10 km
p_1	0.99	Uncertainty on event location—before 1970—horizontal	15 km
x_k	0.2	Uncertainty on event location—before 1970—vertical	20 km
x_{meff}	4.5		
r_{fact}	20		

τ_{min}/τ_{max}, look-ahead time window for building clusters; p_1, probability of detecting the next clustered event; r_{fact}, number of crack radii surrounding each earthquake within which to consider linking a new event into the cluster; x_k, coefficient for mainshock magnitude; x_{meff}, the minimum magnitude cutoff for the catalog.

we can obtain the value of M_{max} from the recurrence parameters a, b, and $\dot{M}_{0G}$:

$$M_{max} = \frac{1}{c-b}\left(\log_{10}(\dot{M}_{0G}) - \log_{10}\left(\frac{b}{c-b}\right) - a - d\right). \quad \text{(A8)}$$

Some authors use $d = 9.0$ or $d = 9.05$, depending on how the coefficients are rounded in the equation relating moment and moment magnitude (see, e.g., Pancha *et al.*, 2006). Using $d = 9.0$ rather than $d = 9.1$ leads to a 20% decrease in the value of the moment rate, for a given magnitude.

Discrete noncumulative rates for Gutenberg–Richter forms 1–3

The distributions of Figure A1 correspond to the discrete noncumulative seismic rates of Forms 1–3 in Anderson and Luco (1983). The recurrence parameters have been determined for the Esmeraldas source zone ($a = 3.35$, $b = 0.67$); an M_{max} of 8.6 is considered. These distributions are provided as input to the OpenQuake hazard engine, to describe occurrence rates of earthquakes on the Esmeraldas dipping plane. The only difference between Forms 1 and 2 lies in the last magnitude interval (see fig. 1B and text page 474 in Anderson and Luco, 1983).

TABLE A3
Time Windows of Completeness Established for Interface Events in Ecuador and Number of Events Falling within the Time Windows of Completeness for Esmeraldas Source Zone

Magnitude Interval	Time Window of Completeness	Number of Events before Declustering	Number of Events after Declustering
[4.5–4.8]	1967–2017	89	33
[4.8–5.1]	1964–2017	90	41
[5.1–5.4]	1964–2017	30	13
[5.4–5.7]	1964–2017	24	14
[5.7–6.0]	1950–2017	11	5
[6.0–6.3]	1920–2017	18	7
[6.3–6.6]	1920–2017	8	7
[6.6–6.9]	1900–2017	10	6
[6.9–7.2]	1900–2017	3	3
[7.2–7.5]	1900–2017	0	0
[7.5–7.8]	1900–2017	2	2
[7.8–8.1]	1900–2017	2	2
[8.1–8.4]	1900–2017	0	0
[8.4–8.7]	1900–2017	1	1

Manuscript received 22 October 2020
Published online 27 April 2021